

# Progress report on the Åforsk project “Development of sustainable activated carbons from nanocellulose for industrial CO<sub>2</sub> capture and volatile organic compounds removal (ref. nr. 18-413)”

Chao Xu

Division of Nanotechnology and Functional Materials  
Department of Engineering Science, Ångström Laboratory  
Uppsala University  
751 21 Uppsala, Sweden  
Email: [chao.xu@angstrom.uu.se](mailto:chao.xu@angstrom.uu.se)

## Summary

The granted Åforsk project had been well implemented in 2018 at Uppsala University, which had led to many promising research results and three high-impact papers published in *Journal of Materials Chemistry A*, *Chemistry – A European Journal*, and *Nanomaterials*. The project had mainly focused on the development of sustainable nanocelluloses and their nanocomposites for environmental and energy related applications. The research results indicate that nanocelluloses can be used as raw materials to prepare porous carbon aerogels for CO<sub>2</sub> capture and volatile organic compounds (VOC) adsorption, and as flexible templates or substrates to fabricate other functional materials with formation of novel nanocomposites for the uses in electrochemical energy storage, and VOC removal, etc. We believe that the outcomes from this project not only contribute to the fundamental research in nanocelluloses and functional nanomaterials, but also would greatly promote the practical applications of nanocelluloses-based materials.

The research results are divided into the following three parts:

### **Part 1. All nanocellulose-based aerogel for CO<sub>2</sub> capture and VOC adsorption**

*(Unpublished results, manuscript in preparation)*

Our preliminary studies (C. Xu et al., *Advanced Sustainable Systems*, **2018**, 2, 201700147) have demonstrated that direct carbonization of *Cladophora* cellulose (a type of nanocellulose extracted from algae) could prepare porous carbons with relatively high surface areas and narrow micropores. However, the obtained porous carbons were in the form of fine powders, which were difficult to handle for practical applications. In this context, we have developed freestanding porous carbon aerogel based on nanocelluloses, displaying ultrahigh sorption capacities for organic liquids. Specifically, the porous carbons derived from nanocelluloses were first treated with acid to modify the surface. The modified porous carbons with significantly increased hydrophilicity were homogeneously dispersed with nanocellulose in water. Following, freeze-drying of the mixture formed a freestanding nanocellulose-porous carbon aerogel (NPCA) (Figure 1). The aerogel had a dimension of 2.3 cm × 1.5 cm (diameter × height) and a low density of 3 mg/cm<sup>3</sup>. Remarkably, the ultralight aerogel demonstrated very strong mechanical strength. As clearly seen from *Figure 1*, the volumetric deformation the aerogel (0.01 g) was less than 10 % when a glass bottle (8.03 g, 803 times heavier than the aerogel) was placed on the top of the aerogel. The high mechanical strength of the aerogel can be attributed to its highly cross-linked nanostructure as observed in the SEM images.

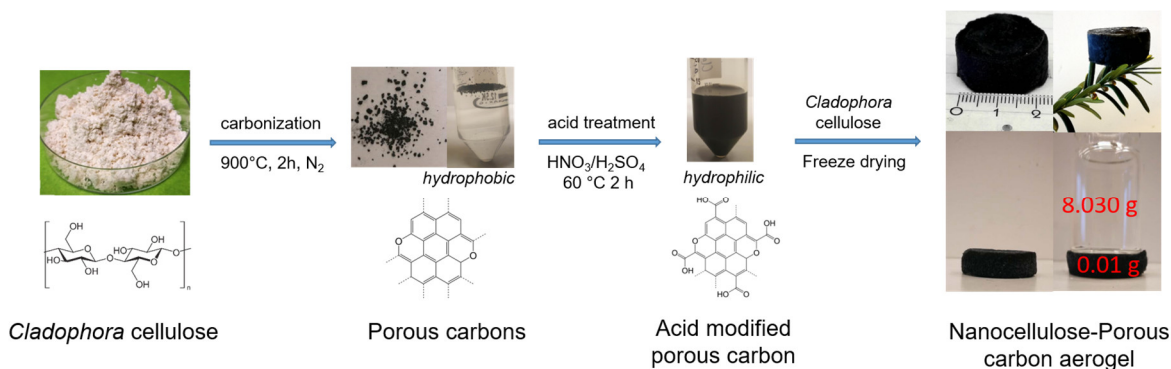


Figure 1. Preparation of nanocellulose-porous carbon aerogel from Cladophora cellulose.

The morphology of the modified porous carbon and the aerogel were revealed by scanning electron microscopy (SEM). The porous carbon had a flower-like morphology consisting of uniform nanofibers with a diameter of  $\approx 30$  nm (Figure 2a-b). The nano-flowers of porous carbon with high hydrophilicity were homogeneously dispersed and cross-linked by nanocelluloses, forming the mechanically strong aerogel (Figure 2c-d). The aerogel had a relatively high specific surface area of 238 m<sup>2</sup>/g according to the N<sub>2</sub> sorption measurement. Pore size distribution analysis showed that the aerogel contained both micropores and mesopores, which arose from the porous carbon and the inter-fibers of nanocelluloses, respectively (Figure 3). The micropores would contribute to the high adsorption capacity for CO<sub>2</sub> and VOCs, while the mesopores would facilitate the mass transfer and enhance the sorption kinetics.

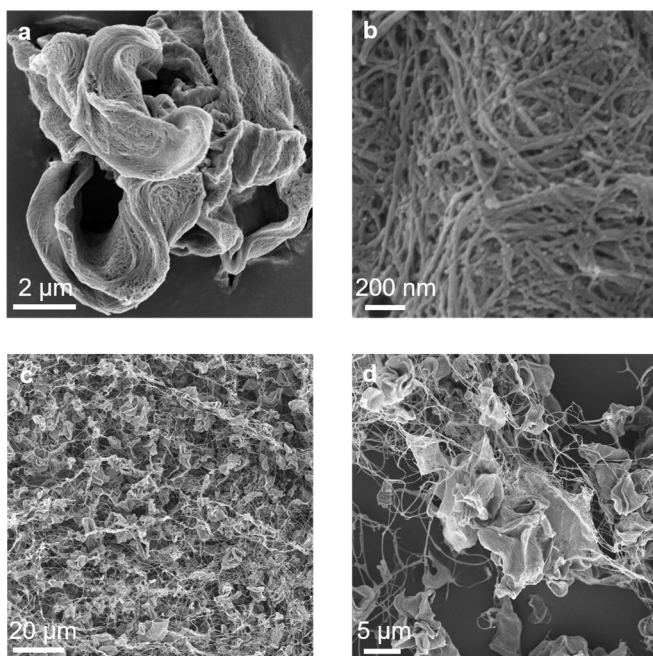


Figure 2. SEM images of (a-b) acid treated porous carbon, and (c-d) of nanocellulose-porous carbon aerogel (NPCA) at different magnifications

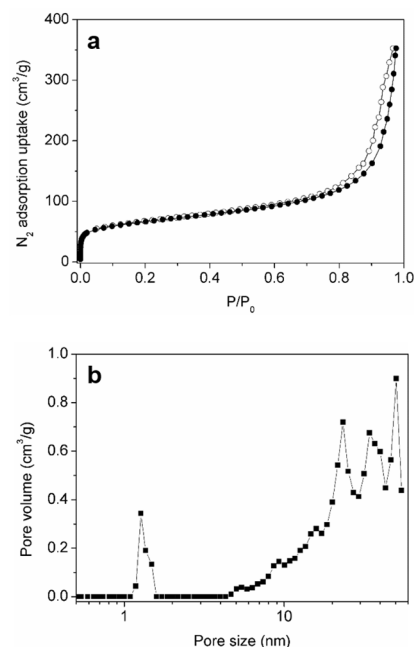


Figure 3. (a) N<sub>2</sub> sorption isotherms of nanocellulose-porous carbon aerogel (NPCA) at 77 K and (b) its pore size distributions

CO<sub>2</sub> adsorption studies showed that the aerogel had relatively high CO<sub>2</sub> adsorption capacities of 1.75 mmol/g at 1 bar, 0.90 mmol/g at 0.15 bar and 273 K. In contrast, it had much lower N<sub>2</sub> uptakes at the same conditions (*Figure 4a*). Based on the single component adsorption data, CO<sub>2</sub>-over-N<sub>2</sub> selectivity of the aerogel was calculated to estimate its ability for post-combustion capture of CO<sub>2</sub>. The calculation revealed that the aerogel had a high CO<sub>2</sub>-over-N<sub>2</sub> selectivity of 52 for a simulated gas mixture containing 15 v% of CO<sub>2</sub> and 85 v% of N<sub>2</sub> at 273 K. The high CO<sub>2</sub> uptake can be attributed to the micropores of the porous carbon that could form strong interactions with CO<sub>2</sub> molecules. The high CO<sub>2</sub>-over-N<sub>2</sub> selectivity can be ascribed to molecular sieving effect of the micropores and/or the thermodynamic effect.

Owing to the hierarchical porous structure of the aerogel, it was tested as sorbent for various organic liquids. Five typical organic liquids (chloroform, acetone, tetrahydrofuran, benzene, toluene), the most common organic pollutants in air and water, were employed for the sorption study. As illustrated in *Figure 4b*, the aerogel displayed very high adsorption capacities of 100-217 times of its own weight for the selected organic liquids.

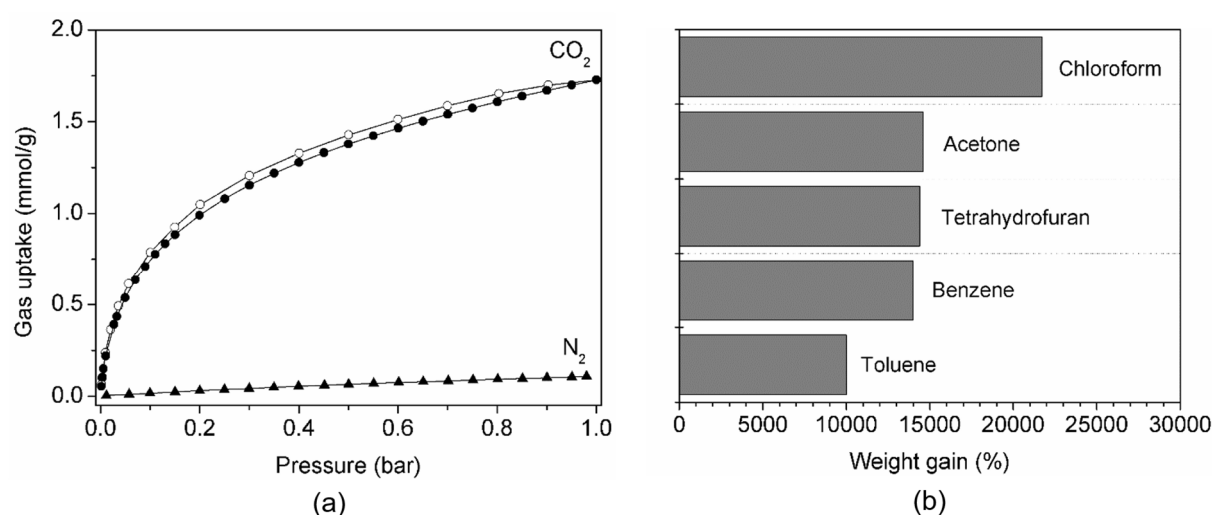


Figure 4. (a) CO<sub>2</sub> and N<sub>2</sub> adsorption isotherms of the nanocellulose-porous carbon aerogel recorded at 273 K and 0-1 bar; (b) Adsorption capacities of the aerogel for various organic liquids. Weight gain means the weight ratio of the adsorbed liquid to the aerogel.

To conclude, we have developed a facile approach to process nanocellulose-based porous carbon powders into freestanding hybrid aerogels with the assistance of raw nanocelluloses. It is noteworthy that the hybrid aerogel is composed by all cellulose-based components, which is a great advantage for the development of nanomaterials from the sustainable and environmental friendly point of view. This study not only provides a sustainable approach to prepare porous carbons, but also brings up new ideas for processing and shaping porous carbon materials that may open up their practical applications in CO<sub>2</sub> capture, air and water purification, etc.

Separately, we have written a review paper entitled “Sustainable Porous Carbon Materials Derived from Wood-Based Biopolymers for CO<sub>2</sub> Capture”, which was published in *Nanomaterials* (**Chao Xu\*** and Maria Strømme, *Nanomaterials* **2019**, *9*, 103). This review paper introduces the general conversion routes of wood-based biopolymers including cellulose, hemicellulose and lignin to porous carbons and the conversion mechanisms. The relationship between CO<sub>2</sub> adsorption behaviors (e.g., CO<sub>2</sub> adsorption capacity, CO<sub>2</sub>-over-N<sub>2</sub> selectivity, kinetics) and nanostructures (e.g., porosity, composition) of the biopolymer-based porous carbons are summarized. We also present our perspectives on the challenges and future developments of using sustainable porous carbon materials in carbon capture and separation.

## Part 2. Highly Transparent, Flexible, and Mechanically Strong Nanopapers of Cellulose Nanofibers @Metal–Organic Frameworks

Shengyang Zhou, Maria Strømme,\* and **Chao Xu**,\* *Chemistry – A European Journal*, 2019, DOI: 10.1002/chem.201806417. **HOT PAPER!!!**

Metal-organic frameworks (MOFs) is an emerging family of porous materials constructed by linking inorganic metal-containing nodes and organic ligands. Because of their high surface areas (up to 7000 m<sup>2</sup>/g), tunable pore sizes, rich functionalities, and synthetic diversity, MOFs have great potential applications in gas storage and separation, air and water purification, energy storage and conversion, catalysis, etc. However, MOFs synthesized from conventional methods, usually in the form of powder, are difficult for processing (e.g., structuring, shaping) because of their insoluble and brittle properties. As a result, the practical applications of MOFs are significantly hampered.

In this context, we have developed a simple, controllable, and scalable approach to process a range of MOFs into freestanding nanopapers with the assistance of cellulose nanofibers (CNFs). Continuous MOF nanolayers with thickness of 3–5 nm were grown on the surface of carboxylated CNFs by interfacial reactions, with the charge density on the surface of the CNFs and the dosage of the surfactant polyvinylpyrrolidone (PVP) being carefully adjusted (*Figure 5a*). Further assembly of the hybrid nanofibers obtained freestanding nanopapers of CNF@MOF (*Figure 5b*). SEM studies revealed that CNFs were uniformly wrapped by continuous MOF nanolayers rather than aggregated MOF nanoparticles, while the nanopapers composed of homogeneously stacked nanofibers of CNF@MOF.

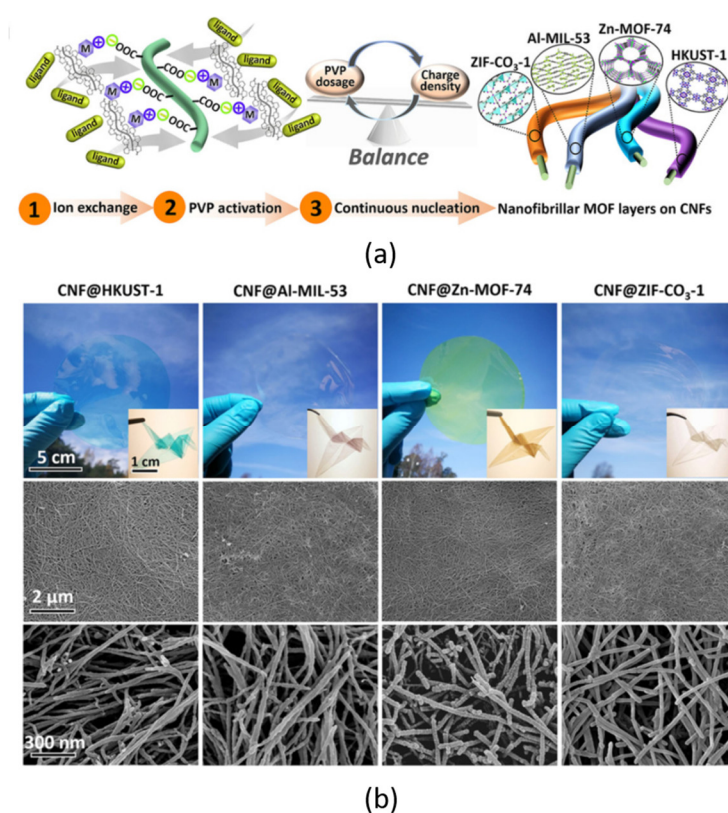


Figure 5. a) Schematic illustration of the synthesis procedures for the hybrid nanofibers of CNF@MOF. b) Photographs and SEM images of the four types of CNF@MOF nanopapers (Reproduced from *Chem. Eur. J.*, 2019, DOI: 10.1002/chem.201806417, with permission from Wiley, 2019)

Because of the unique nanostructure of the hybrid nanofibers of CNF@MOF, the nanopapers can be folded and cut into complex shapes, demonstrating good flexibility and processability. The nanopapers were highly transparent displaying transmittance up to 90 % in the visible region (400 – 800 nm), which was much higher than that of state-of-the-art transparent composites based on CNFs. In addition, the nanopapers showed very strong mechanical strength with tensile strength of up to 589.8 MPa and Young's modulus of up to 31.6 GPa. Furthermore, the thermal stability of the MOF and CNF components in the nanopapers were enhanced in comparison to the pure MOF and CNF.

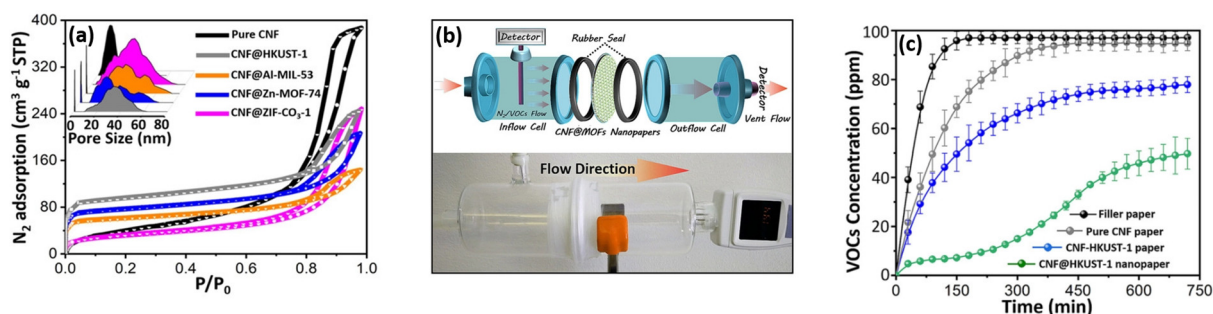


Figure 6. (a)  $N_2$  sorption isotherms of CNF@MOF nanopapers measured at 77 K and the calculated pore size distributions; (b) Schematic illustration and photograph of the home-designed apparatus for VOC separation test; (c) The curves of VOC concentration vs. time at the outlet of the apparatus using normal filter paper, CNF paper, CNF-HKUST-1 paper and CNF@HKUST-1 nanopaper as the VOC filter. HKUST-1 is a typical MOF. (Reproduced from *Chem. Eur. J.*, 2019, DOI: 10.1002/chem.201806417, with permission from Wiley, 2019)

The porosity of the nanopapers were analyzed by  $N_2$  sorption measurement, revealing that the nanopapers had relatively high surface areas up to  $281 m^2/g$  and contained both micropores and mesopores. Given the hierarchical porous and nanofibrous structure and the excellent mechanical properties, we have developed a proof-of-concept study of VOC separation for the freestanding CNF@MOF nanopapers (Figure 6). The study demonstrated that the CNF@MOF nanopapers had superior separation efficiency for VOCs compared to normal filter paper, pure CNF paper, and CNF-MOF paper (CNFs and MOF nanoparticles were physically mixed). We believe that this study of VOC separation by CNF@MOF nanopapers moves a significant step towards the practical application for MOFs and MOF-based nanocomposites. This study offers new avenues for processing, shaping, and structuring MOF materials with sustainable nanocellulose that may boost their practical applications in separation procedures, sensors, thermal insulators, fire retardants, etc.

### Part 3. Interweaving metal–organic framework-templated Co–Ni layered double hydroxide nanocages with nanocellulose and carbon nanotubes to make flexible and foldable electrodes for energy storage devices

Chao Xu,\* Xueying Kong, Shengyang Zhou, Bing Zheng,\* Fengwei Huo and Maria Strømme\*, *Journal of Materials Chemistry A*, 2018, 6, 24050-24057.

The growing demands of flexible electronics such as foldable phones, roll-up displays, and wearable devices have attracted great interests in developing high performance, thin, flexible, lightweight, environmentally friendly energy storage devices (ESDs). Metal-organic frameworks (MOFs) with high surface areas and predetermined architectures have been recently studied for electrochemical energy storage. Their ordered porous channels and high surface areas facilitate fast diffusion of the electrolyte and the built-in transition metal ions or clusters can deliver electrochemical activity. However, the drawback of low processability of MOFs has significantly limited their applications in flexible ESDs.

In this study, we introduce an assembly approach for interweaving *Cladophora* cellulose (CC) nanofibers, multi-walled carbon nanotubes (CNTs), and ZIF-67 (a cobalt-based MOF) nanocrystals into a freestanding, flexible, and foldable nanosheet (Figure 7). The ZIF-67 nanocrystals can be converted into Co–Ni layered double hydroxide (LDH) nanocages, a well-known electrochemically active material. The structures of the nanosheets were fully characterised by powder X-ray diffraction, X-ray photoelectron spectroscopy, and X-ray energy dispersive spectroscopy. The morphology of the ZIF–CC–CNT and LDH–CC–CNT nanosheets studied by SEM revealed the interconnections between the ZIF-67 or LDH nanocrystals, the CC nanofibers, and the CNTs (Figure 8). The nanocrystals were uniformly dispersed and interwoven by the cross-linked CC nanofibers and CNTs to form the framework of the nanosheets. We believe that CC nanofibers play a key role in the formation of such interconnected nanostructures because of their ability to aid in the dispersion and intertwining of the nanocrystals.

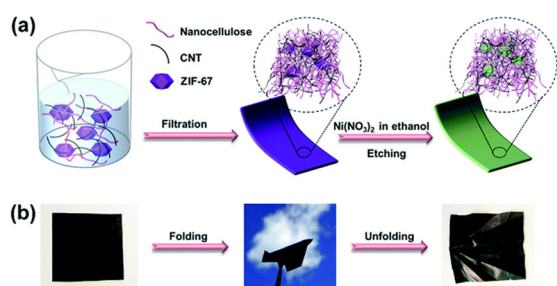


Figure 7. (a) Schematic illustration of the formation process of LDH–CC–CNT nanosheets; (b) optical images of a flexible, foldable LDH–CC–CNT nanosheets.

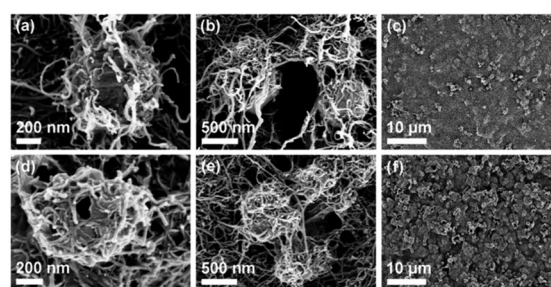


Figure 8. Scanning electron microscopy images of (a–c) ZIF–CC–CNT and (d–f) LDH–CC–CNT nanosheets at different magnifications.

(Reproduced from *J. Mater. Chem. A.*, 2018, 6, 24050, with permission from The Royal Society of Chemistry, 2018)

Electrochemical studies indicated that the LDH–CC–CNT nanosheets were battery-type electrodes, which had very high specific areal capacitances of up to 1979 mF/cm<sup>2</sup> at a current density of 1 mA/cm<sup>2</sup>. The active material LDH in the nanosheets had very high gravimetric capacitances of up to 1287 F/g, which was much higher than those reported values. The high capacitances can be attributed to the unique nanostructure that the conductive and interwoven framework facilitating effective electron transfer and the hierarchical porous structures enabling faster diffusion of the electrolyte.

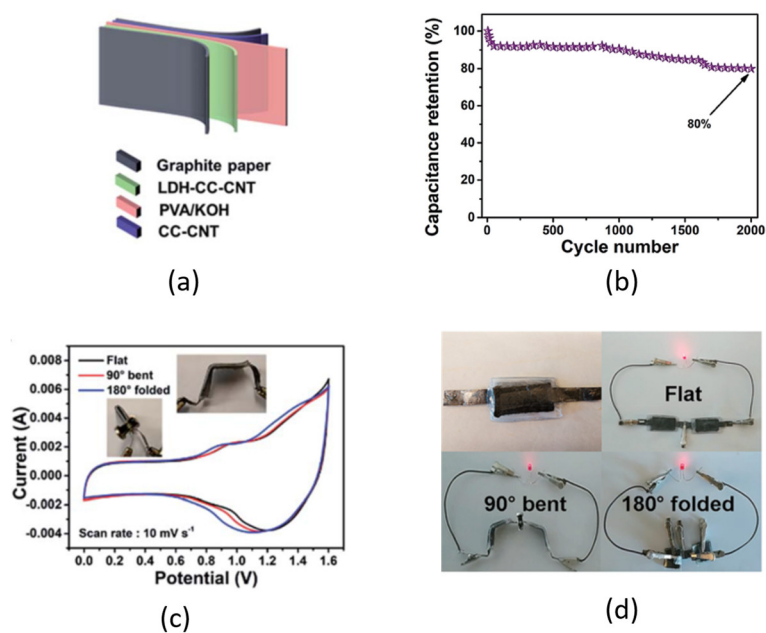


Figure 9. (a) Schematic illustration of the flexible and solid-state hybrid electrochemical energy storage device LDH-CC-CNT//CC-CNT; (b) Cycling performance of the device; (c) CV curves of the device under different bending conditions; (d) Photo of red LEDs powered by the bent or folded device. (Reproduced from *J. Mater. Chem. A.*, 2018, 6, 24050, with permission from The Royal Society of Chemistry, 2018)

Given the high electrochemical performance and the high flexibility, we assembled a flexible, foldable, and all-solid-state hybrid ESD based on LDH-CC-CNT electrodes. (Figure 9) The device displayed a high areal capacitance of  $168 \text{ mF/cm}^2$  at a discharge current density of  $1 \text{ mA/cm}^2$ . In addition, the hybrid device retained more than 80 % of its original capacitance after 2000 cycles. Remarkably, the devices in the series can light the LED even when they were bent and folded, which demonstrated excellent flexibility and foldability of the device. This study may open a window for the development of flexible, foldable, lightweight, and high-performance electronic energy storage devices based on MOF-related materials and sustainable cellulose.

## Nanotechnology | Hot Paper

## Highly Transparent, Flexible, and Mechanically Strong Nanopapers of Cellulose Nanofibers @Metal–Organic Frameworks

Shengyang Zhou, Maria Strømme,\* and Chao Xu\*[a]

**Abstract:** Freestanding nanopapers were fabricated by the assembly of metal–organic frameworks (MOFs) onto cellulose nanofibers (CNFs). The CNFs are wrapped by continuously nucleated MOF layers (CNF@MOF) by interfacial synthesis, with the charge density on the surface of the CNFs and the dosage of the surfactant polyvinylpyrrolidone (PVP) being carefully adjusted. The obtained CNF@MOF nanofibers with long-range, continuous, hybrid nanostructures were very different to the composites formed by aggregation of MOF nanoparticles on the substrates. Four typical MOFs (HKUST-1, Al-MIL-53, Zn-MOF-74, ZIF-CO<sub>3</sub>-1) were successfully grown onto CNFs in aqueous solutions and further fabricated into freestanding nanopapers. Because of their unique nanostructures and morphologies, the corresponding flexible nanopapers exhibit hierarchical meso-micropores, high optical transparency, high thermal stability, and high mechanical strength. A proof-of-concept study shows that the CNF@MOF nanopapers can be used as efficient filters to separate volatile organic compounds (VOCs) from the air. This work provides a new path for structuring MOF materials that may boost their practical application.

As an emerging family of crystalline porous materials, metal–organic frameworks (MOFs) are coordination polymers constructed by linking inorganic metal-containing nodes and organic ligands.<sup>[1]</sup> Among the attractive features of MOFs are the diverse design principles based on reticular chemistry, which allows for precise control of their porosity and functionality.<sup>[2]</sup> Significant efforts have been made to design MOFs with novel crystal structures at the molecular level. By careful selection of the matrix of inorganic and organic building blocks, thousands of MOFs have been successfully synthesized in recent years.<sup>[3]</sup> Accordingly, their potential application in gas storage and separation, air and water purification, energy storage, catalysis, and etc. are well investigated.<sup>[4]</sup> However, significant challenges

in controlling the morphology, dimensions, and alignment of MOF crystals at the microscopic level remain.<sup>[5]</sup> Moreover, MOF crystals synthesized by conventional methods lack processability because they are insoluble and brittle.<sup>[6]</sup> As a result, some valuable properties of MOFs (e.g., optical, mechanical) remain undetermined and their industrial application is hampered.

Recently, template-assisted synthesis of MOFs has been suggested as a feasible approach to structuring MOFs.<sup>[7]</sup> In general, MOF crystals are deposited onto-or grown on-the surface of the substrate by interfacial interactions with bottom-up synthesis, in which the structure and the surface chemistry of the substrate play a key role in the growth of MOF crystals.<sup>[8]</sup> With this method, MOFs with various architectures (e.g., zero-dimensional MOF nanospheres, one-dimensional MOF nanofibers, and two-dimensional MOF films) have been fabricated on different substrates.<sup>[9]</sup> However, these methods are wholly reliant on the nanostructure of the substrates, which are not suitable for all types of MOFs. Meanwhile, the complicated procedure hampers the large-scale preparation of the target materials.

Cellulose nanofibers (CNFs) are naturally abundant biopolymers, which possess a 1D nanostructure and offer potential for chemical modification and physical processing. Therefore, they are considered feasible templates for the preparation of fibrous nanomaterials.<sup>[10]</sup> Recently, a few reports on hybrid composites incorporating MOF particles with CNFs or cellulose-based papers have been published.<sup>[11]</sup> With the combined properties of MOFs and CNFs, these composites demonstrate high performance in gas separation and the removal of organic dye molecules and heavy metal ions from polluted aqueous solutions. However, the CNFs only serve as substrates for loading MOFs in the fabrication of composites in which MOF particles are dispersed in the matrix or aggregated on the surface of CNFs. It would be desirable, yet challenging, to grow MOFs with controlled morphology on CNFs toward chemically integrated hybrids of CNF@MOF with easy processability and shapeability for the development of their practical applications.

We demonstrate a simple, controllable, and scalable approach to growing continuous MOF layers on ultrafine CNFs by interfacial reactions. The obtained hybrid nanofibers of CNF@MOF have interconnected nanostructures assembled by wrapping CNFs with MOF layers. This strategy relies on the synergetic effect of the carboxylated CNFs and the surfactant of polyvinylpyrrolidone (PVP) used for the synthesis. Four typical crystalline MOFs (HKUST-1, Al-MIL-53, Zn-MOF-74, ZIF-CO<sub>3</sub>-1), were successfully induced into nanofibrillar layers on the

[a] S. Zhou, Prof. M. Strømme, Dr. C. Xu  
Nanotechnology and Functional Materials  
Department of Engineering Sciences  
Ångström Laboratory, Uppsala University, 751 21 Uppsala (Sweden)  
E-mail: maria.stromme@angstrom.uu.se  
chao.xu@angstrom.uu.se

Supporting information and the ORCID identification number(s) for the author(s) of this article can be found under:  
<https://doi.org/10.1002/chem.201806417>.

surface of CNFs in aqueous solution. Because of the simple process and cheap starting materials, the hybrid nanofibers of CNF@MOF can be prepared on a large scale and further assembled into freestanding, flexible nanopapers that exhibit hierarchical porosity, high transparency, high thermal stability, and high mechanical strength.

Figure 1 a illustrates the synthesis procedures for CNF@MOF. *Cladophora* cellulose extracted from algae and its oxidized derivatives with nanofibrillar structures (Figures S1 and S2) were applied as CNFs for the fabrication of MOFs. Briefly, the aqueous suspension of carboxylated CNFs with optimized charge density (Table S1, Supporting Information) were first ion-exchanged with metal ions; then a moderate amount of PVP was added to the suspension to modify the surface of the CNFs; and after that, a certain proportion of metal salts and organic ligands were added dropwise while stirring. Continuous growth of various MOFs (HKUST-1, Al-MIL-53, Zn-MOF-74, ZIF-CO<sub>3</sub>-1) into nanofibrillar layers along the CNFs can thus be achieved by tuning the charge density (the degree of carboxylation) of CNFs and the dosage of PVP. Powder X-ray diffraction (XRD) analysis confirms (Figure S3, Supporting Information) the

high crystallinity and the composition of the MOFs in CNF@MOF as compared to the XRD patterns of the corresponding pure MOFs (Figure S4, Supporting Information).<sup>[12]</sup> The strong diffraction peaks at 13.1 (100), 15.2 (010), and 20.2° (110) indicate the high crystallinity of CNFs. Detailed synthesis procedures for various CNF@MOF are provided in the Supporting Information.

To control the growth of the MOFs on CNFs, we carried out series of experiments to investigate the effects of the charge density of CNFs and the dosage of PVP on the morphology of the MOFs growing on CNFs. Taking CNF@HKUST-1 as an example, CNFs with variable charge densities (0, 326, 664, 1301  $\mu\text{mol g}^{-1}$ ) and PVP with different dosages (0, 20, 40, 80  $\mu\text{mol g}^{-1}$ ) were applied in the synthesis. Figure 1 b compares SEM images of the samples prepared with different charge densities on the CNFs and dosages of PVP. In the absence of PVP, isolated HKUST-1 nanocrystals were formed and physically dispersed within the matrix of the unmodified CNFs (without carboxyl groups the charge density is 0) (Figure 1 b 1). In comparison, HKUST-1 nanoparticles were attached to the surface of the CNFs when the charge density was 326  $\mu\text{mol g}^{-1}$  (Fig-

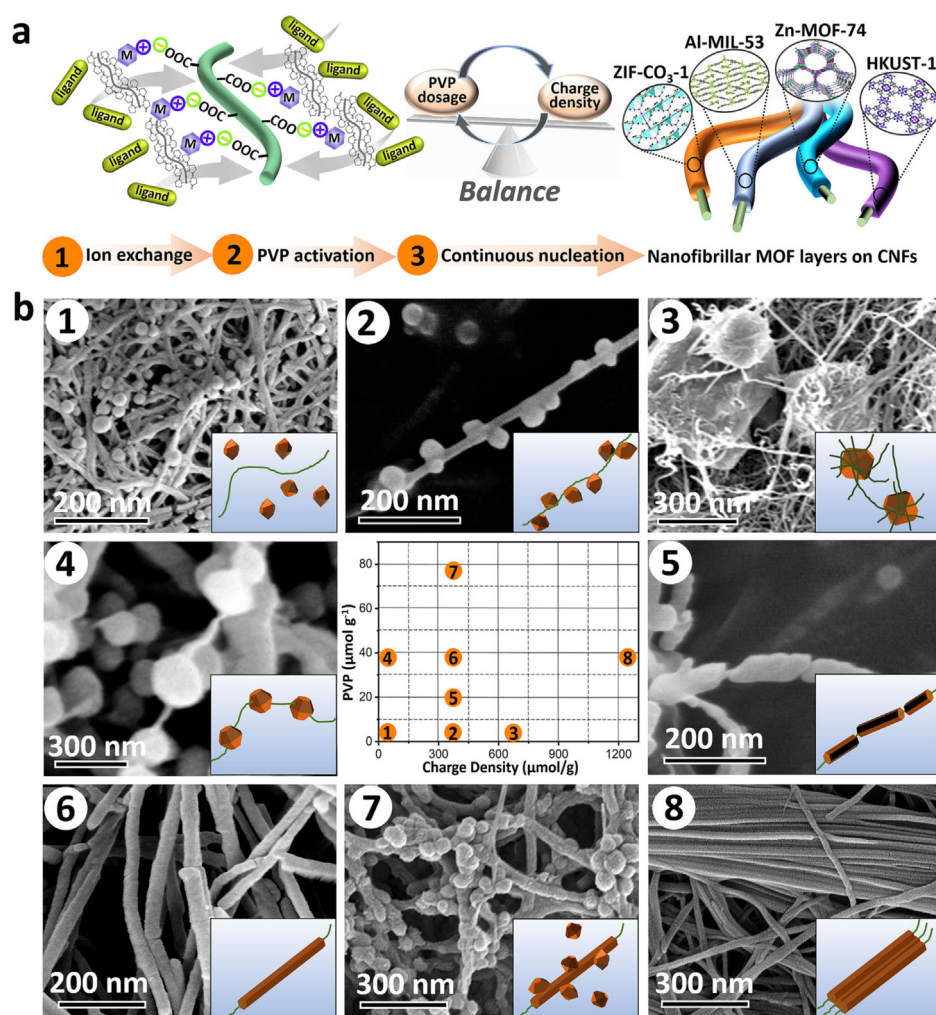


**Figure 1.** a) Schematic illustration of the synthesis procedures for the hybrid nanofibers of CNF@MOF. b) SEM images of CNF@HKUST-1 prepared by different parameters clearly show the effect of the charge density of CNFs and the dosage of PVP on the morphology of the hybrid nanofibers.

ure 1 b2). Further increasing the charge density of CNFs to  $664 \mu\text{mol g}^{-1}$  resulted in a nanostructure of HKUST-1 nanoparticles intertwined with a number of CNFs (Figure 1 b3). Such interconnected nanostructures confirm that the carboxyl groups on the CNFs with a high charge density could increase the interactions between the CNFs and the MOFs. The amphiphilic surfactant PVP has earlier been shown to regulate the growth and crystallization of MOFs and to enable the encapsulation of nanomaterials, including metal oxides, metals and graphene oxide, by interfacial activation and stabilization.<sup>[13]</sup> Therefore, PVP was used to facilitate the crystallization of MOF onto CNF for the synthesis of CNF@MOF in this study. We found that unmodified CNFs can assemble isolated HKUST-1 nanocrystals to form typical “shish-kebab” nanostructures in the presence of PVP ( $40 \mu\text{mol g}^{-1}$ ); however, the HKUST-1 nanocrystals remained separate due to the weak bonding ability of the unmodified CNFs (Figure 1 b4). The HKUST-1 nanocrystals, acting as the kebab, tend to convert into rodlike crystals coating the shish of carboxylated CNFs in the presence of PVP (Figure 1 b5). Similar nanostructures have been observed in CNT-ZIF-8, in which ZIF-8 nanocrystals were connected by CNTs with the assistance of PVP.<sup>[14]</sup> By carefully adjusting the charge density of the CNFs ( $326 \mu\text{mol g}^{-1}$ ) and the amount of PVP ( $40 \mu\text{mol g}^{-1}$ ) used for the synthesis, the integrated hybrid nanofibers of CNF@HKUST-1 with continuous HKUST-1 layers growing on the CNFs were ultimately fabricated as the result of a synergetic effect of carboxylated CNFs and PVP on the crystallization of HKUST-1 (Figure 1 b-6). However, an excess dosage of PVP ( $80 \mu\text{mol g}^{-1}$ ) led to the formation of extra HKUST-1 nanocrystals attached to the surface of CNF@HKUST-1 (Figure 1 b7). Further increasing the charge density of the CNFs ( $1301 \mu\text{mol g}^{-1}$ ) resulted in bonding CNF@HKUST-1 nanofibers into nanobelts, because of the abundant coordination sites of carboxyl groups on the CNFs (Figure 1 b8). With this procedure, we can easily optimize the parameters for growing

other types of MOFs (Al-MIL-53, Zn-MOF-74, ZIF-CO<sub>3</sub>-1) with continuous layered nanostructures on CNFs (Table S2), which demonstrates the universality of the synthetic strategy for the fabrication of such hybrid nanofibers of CNF@MOF. Noteworthy is that the obtained CNF@MOF fibers have very different nanostructures and properties from those of reported cellulose-MOF composites. Table S3, Supporting Information, compares the synthesis methods, morphologies, and properties for the MOF-cellulose composites reported in the references with those of CNF@MOFs in this study.

For an insight into the mechanism of forming the continuous MOF layers on CNFs, we correlated the zeta-potential values of the obtained samples to their synthesis parameters (the charge density of CNFs and the dosage of PVP) and morphologies, as shown in Figure S5, Supporting Information. The zeta potential of CNFs with different charge densities and pure MOFs were measured in a neutral aqueous solution—the values are listed in Table S4, Supporting Information. Obviously, the carboxylated CNFs show negative zeta potential values because of the negatively charged carboxyl groups on the surface. The negative zeta potentials were dramatically shifted to positive values for CNF@MOF, when the surface of the CNFs was entirely covered by MOF layers. This is expected since the pendent carboxyl groups on the CNFs were charge-balanced by metal ions via coordination. In comparison, the zeta potential values are lower in samples with exposed surface of carboxylated CNFs (Figure 2 b2, 3, 5). It could be speculated that the carboxyl groups on the surface of the CNFs induce the initial crystallization of MOFs and thus bond the CNFs and MOFs together, while the surfactant PVP with amphiphilic nature served as interfacial stabilizer between the CNFs and the MOF layers in the construction of the hybrid nanofibers of CNF@MOF.

Owing to the easy processability of nanocellulose, the hybrid nanofibers of CNF@MOF were further fabricated into

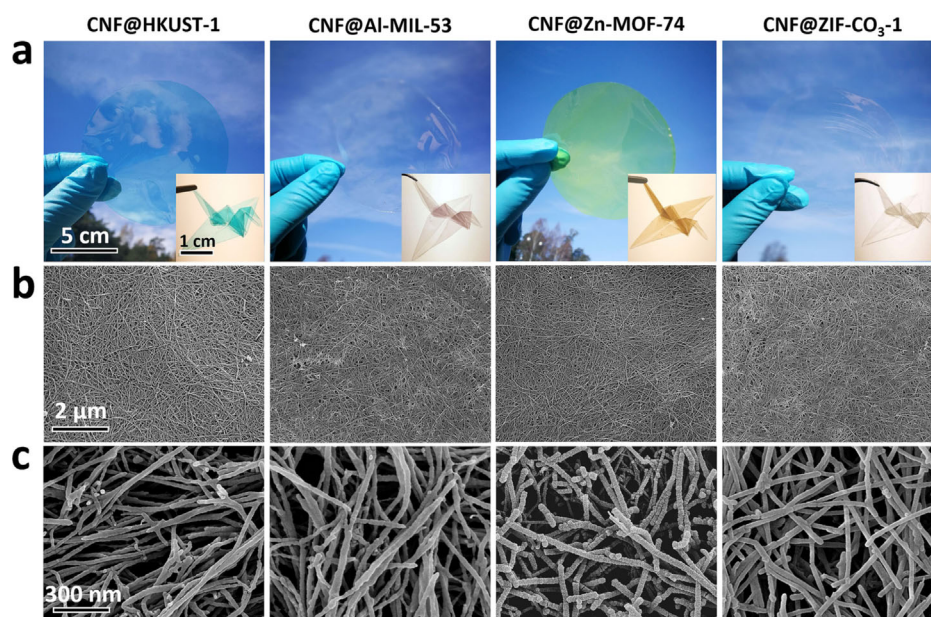


Figure 2. a) Photographs and b, c) SEM images of the four types of CNF@MOF nanopapers.

freestanding nanopapers through the processes of filtration, drying, and mold pressing (Scheme S1, Supporting Information). As shown in Figure 2a, the four types of nanopapers are all highly transparent at optical frequencies at which the color comes from the metal ions or the ligands of the MOFs. Furthermore, these nanopapers show outstanding flexibility, comparable to normal paper. They can be folded (Figure 2a) and cut (Figure S6, Supporting Information) into complex shapes, demonstrating good flexibility and processability. In SEM images of the four types of nanopapers (Figure 2b), we can clearly observe the flat surface of the nanopapers composed of homogeneously stacked nanofibers of CNF@MOF. High-magnification SEM images (Figure 2c) reveal a more detailed microscopic morphology of CNF@MOF. CNFs are uniformly wrapped by MOF layers with a smooth surface rather than having an aggregation of MOF nanoparticles, which confirms the continuous crystallization of MOF induced by the CNFs. CNF@MOF nanofibers have an average diameter of  $\approx 50$  nm, which is significantly thicker than that of pure CNF ( $\approx 20$ – $30$  nm). Furthermore, we have confirmed the structures adopted by CNF@MOF by using TEM image analysis (Figure S7, Supporting Information). The evident contrast between the MOF layer and CNF can be clearly recognized. Energy-dispersive X-ray spectroscopy (EDX) mapping analysis indicates the uniform distribution of metallic elements on the surface of nanofibrillar CNF@MOF.

The porosity of pure CNF paper and CNF@MOF nanopapers was analyzed by  $N_2$  sorption measurements, as illustrated in Figure 3a. The calculated Brunauer–Emmett–Teller (BET) surface areas of CNF@MOF nanopapers ( $219$ – $281$   $m^2 g^{-1}$ , except

for the surface area of CNF@ZIF- $CO_3$ -1, which is  $94$   $m^2 g^{-1}$ ) (Table S5, Supporting Information) are much larger than that of pure CNF paper ( $118$   $m^2 g^{-1}$ ) because of the contribution of the highly microporous MOFs in CNF@MOF. The pore-size distributions in the mesoporous domain were analyzed to gauge the difference in diameter and stacking of the nanofibers. The CNF@MOF nanopapers demonstrate larger mesopores ( $40$ – $50$  nm) than those of the pure CNF paper ( $\approx 20$  nm), indicating the increased diameter of the nanofibers in CNF@MOF.<sup>[15]</sup> These results evidence the core-shell nanostructure of CNF@MOF composed by coating a continuous layer of MOFs on CNFs as observed in the SEM and TEM images.

As shown in Figure 3b, all of the four nanopapers with a  $\approx 25\%$  mass fraction of MOFs show high transmittance up to  $\approx 90\%$  in the visible region ( $400$ – $800$  nm), comparable to that of the pure CNF paper. Remarkably, the transparency of CNF@MOF nanopapers is much higher than that of state-of-the-art transparent composites based on CNFs (Table S6, Figure S10, Supporting Information). The high transparency can be attributed to the specific superstructure of the nanopapers, in which the continuous MOF layers have fewer grain boundaries, while compactly stacking the ultrafine CNF@MOF fibers can reduce the interfiber pore size. As a result, the eliminated absorption, reflection, and scattering of the nanofibers give high transparency to the CNF@MOF nanopapers.<sup>[16]</sup>

The thermal stability of the MOF and CNF components in the CNF@MOF nanopapers are enhanced in comparison to the pure MOF and CNF as verified by TGA (Figure 3c; Figures S11 and S12, Supporting Information). The first onset decomposition temperatures ( $T_d$ ) of CNF@MOF at  $\approx 270$  °C represents the

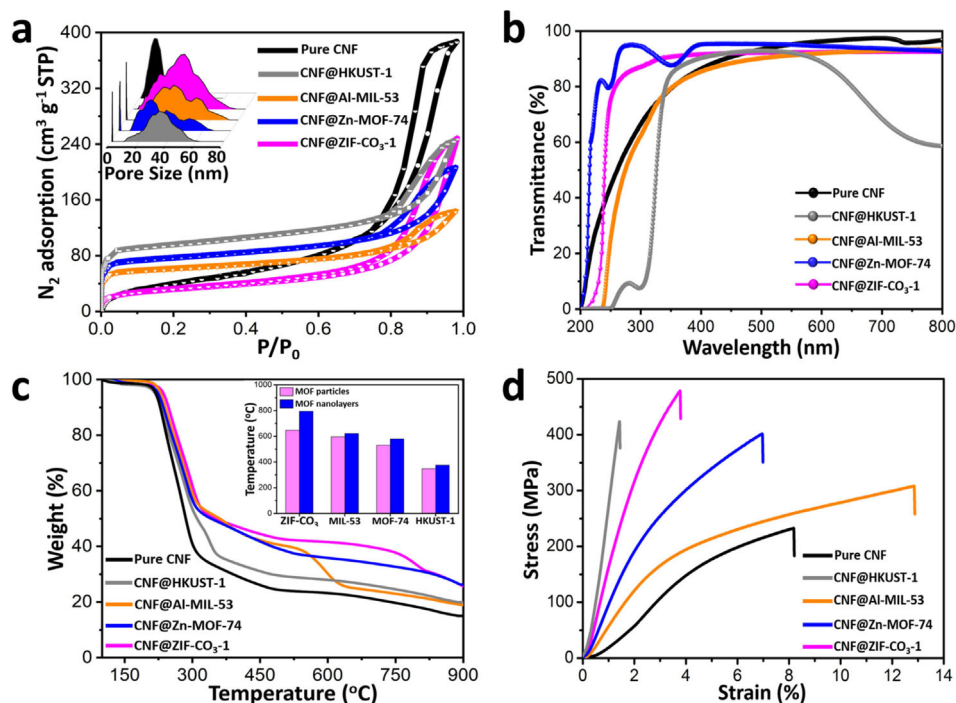


**Figure 3.** Physical properties of CNF@MOF nanopapers: a)  $N_2$  sorption isotherms of CNF@MOF nanopapers measured at 77 K. The inset shows their pore-size distributions calculated from the adsorption branches using a density functional theory model. b) UV/Vis transmittance spectra of CNF@MOF nanopapers. c) Thermogravimetric analysis curves of CNF@MOF nanopapers. The inset compares the onset decomposition temperature of the pure MOF particles and the corresponding MOF components in CNF@MOF nanopapers. d) Strain–stress curves of CNF@MOF nanopapers.

pyrolysis of CNFs, which is slightly higher than the  $T_d$  of pure CNFs ( $\approx 243^\circ\text{C}$ ) due to the protective MOF core layer on the CNFs. The second onset decomposition temperature for CNF@MOF reflects the decomposition of the MOF, which is higher than the  $T_d$  of the corresponding MOF particles. For instance,  $T_d$  increased from  $645^\circ\text{C}$  for ZIF- $\text{CO}_3$ -1 particles to  $792^\circ\text{C}$  for the component of ZIF- $\text{CO}_3$ -1 in the CNF@ZIF- $\text{CO}_3$ -1 nanopaper. The enhanced thermal stability of MOFs in CNF@MOF can be attributed to their continuous layered structures, which increase the surface activation energy in comparison to the individual MOF particles.<sup>[17]</sup>

With the formation of continuous MOF layers on CNFs to make CNF@MOF nanopapers, we are able to evaluate their mechanical properties by tensile measurements.<sup>[18]</sup> As shown in Figure 3 d, the stress–strain curves of the four types of nanopapers evidently tower over the pure CNF paper, which means both the tensile strength and the Young's modulus are improved in the CNF@MOF nanopapers (Figure S13, Supporting Information). Notably, the tensile strength of the CNF@ZIF- $\text{CO}_3$ -1 nanopaper reaches 589.8 MPa and the Young's modulus of the CNF@HKUST-1 nanopaper is as high as 31.6 GPa. These values are significantly higher than those of previously reported CNF-based hybrid composites, such as CNF–carbon nanotubes and CNF–Ag nanowires (Table S7, Supporting Information). More interestingly, thanks to the flexible framework of Al-MIL-53,<sup>[19]</sup> the elongation at break of CNF@Al-MIL-53 exceeds 12%, which is particularly high for CNF-based composites. For comparison, we have also tested the mechanical properties of the CNF-MOF papers, in which CNFs and MOF nanoparticles are physically mixed (Figure S14, Supporting Information). The results revealed the relatively weak mechanical properties of the CNF-MOF papers, displaying a much lower tensile strength ( $< 250$  MPa) and breaking elongation ( $< 6\%$ ) than the values for the CNF@MOF nanopapers. Therefore, we can conclude that the superior mechanical properties of the CNF@MOF nanopapers are ascribed to the integrated nanoarchitectures and the continuous layered MOFs of the hybrid nanofibers.

MOFs are potential VOC sorbents because of their high surface areas and suitable pore sizes. However, most reported studies on MOFs as sorbents focused on the adsorption capacity of MOFs in powder form; not entirely compatible with practical applications for VOC removal from air demanding materials structures of higher mechanical integrity.<sup>[20]</sup> Considering the hierarchical porous and nanofibrillar structure, as well as the excellent mechanical properties, we have developed a proof-of-concept application of VOC separation for the freestanding CNF@MOF nanopapers. The VOC separation ability was investigated using a homemade apparatus as shown in Figure 4a and specified in Figure S15, Supporting Information. Formaldehyde was chosen as a typical VOC source for this study. A  $\text{N}_2$ -diluted VOC gas mixture with a VOC concentration of  $\approx 100$  ppm flowed through the filter, while the VOC concentration at the outlet was dynamically monitored for 12 hours by a VOC detector to evaluate the separation efficiency of the filter (Figure 4b; Figure S16, Supporting Information). CNF@MOF nanopapers, normal filter paper, pure CNF paper, and CNF-

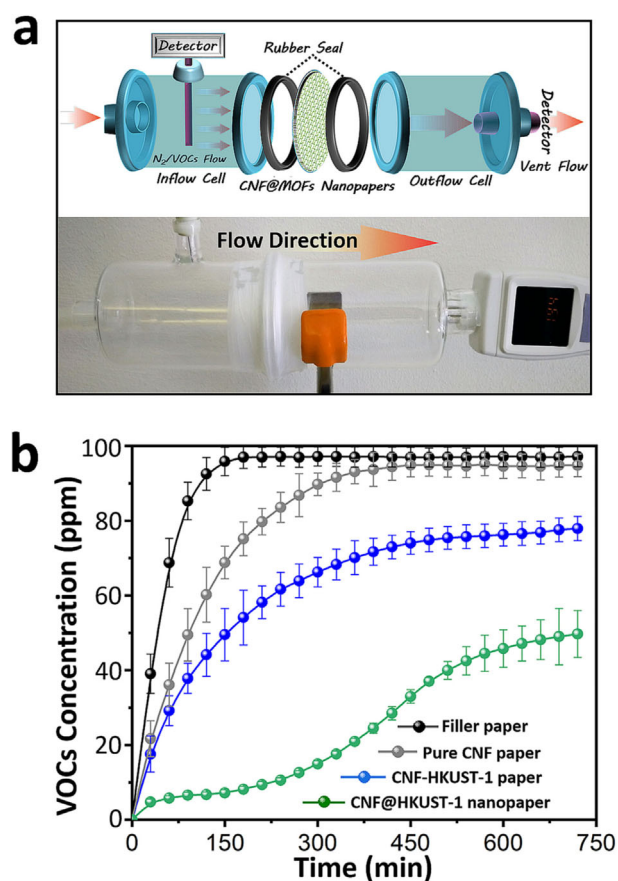


**Figure 4.** a) Schematic illustration and photograph of the home-designed apparatus for VOC separation test. b) The curves of VOC concentration vs. time at the outlet of the apparatus using normal filter paper, CNF paper, CNF-HKUST-1 paper and CNF@HKUST-1 nanopaper as the VOC filter.

MOF papers were applied as the filter, respectively. As expected, normal filter paper showed an extremely weak performance for VOC separation. The VOC concentration at the outlet reached saturation ( $\approx 100$  ppm) very rapidly in under three hours. Similarly, but slightly better, it took  $\approx$  five hours for the pure CNF paper to lose its separation ability. When loading MOF particles on CNFs by physical mixing, the obtained CNF-MOF papers showed improved performance for VOC separation. Taking CNF-HKUST-1 paper as an example, it maintained the function for VOC separation for the full 12 hours; however, the separation efficiency was significantly decreased after three hours and the VOC concentration at the outlet finally reached as high as  $\approx 80$  ppm. In contrast, the CNF@HKUST-1 nanopaper showed superior performance for VOC separation and the separation efficiency faded very slowly during the measurement. The VOC concentration at the outlet stayed below 20 ppm during the first six hours and finally stabilized at  $\approx 50$  ppm. Likewise, other types of CNF@MOF nanopapers demonstrated a high performance for VOC separation (Figure S16, Supporting Information). The strong performance of CNF@MOF nanopapers for VOC separation can be explained by their unique nanostructure and high physicochemical stability (Figure S17, Supporting Information). We believe that this

study of VOC separation by CNF@MOF nanopapers creates a significant move towards the practical application for MOFs and MOF-based nanocomposites.

In conclusion, we have developed a simple method of growing continuous MOF layers on CNFs by interfacial reactions with the formation of hybrid nanofibers of CNF@MOF, which can be further assembled into flexible and freestanding CNF@MOF nanopapers. Because of the unique nanostructures, the nanopapers showed high optical transparency, hierarchical porosity, high thermal stability, and high mechanical strength. Furthermore, the freestanding CNF@MOF nanopapers demonstrated high efficiency for VOC separation. This study offers new avenues for processing, shaping, and structuring MOF materials that may boost their practical applications in separation procedures, sensors, thermal insulators, fire retardants, etc.

## Acknowledgements

The authors acknowledge the Åforsk research grant (18-413). We owe a debt of thanks to Dr. Z. Wang for the discussion on cellulose, to Dr. L. Riekehr and Y. Han for their kind help with TEM measurements, to Dr. J. Yang for helping with the UV and zeta-potential measurements, and to Dr. L. Shi for helping with the mechanical tensile tests.

## Conflict of interest

The authors declare no conflict of interest.

**Keywords:** cellulose nanofibers · interfacial synthesis · metal-organic frameworks · nanopapers · VOC separation

- [1] S. Kitagawa, R. Kitaura, S. Noro, *Angew. Chem. Int. Ed.* **2004**, *43*, 2334–2375; *Angew. Chem.* **2004**, *116*, 2388–2430.
- [2] O. M. Yaghi, M. O’Keeffe, N. W. Ockwig, H. K. Chae, M. Eddaoudi, J. Kim, *Nature* **2003**, *423*, 705–714.
- [3] S. T. Meek, J. A. Greathouse, M. D. Allendorf, *Adv. Mater.* **2011**, *23*, 249–267.
- [4] a) J. R. Li, J. Sculley, H. C. Zhou, *Chem. Rev.* **2012**, *112*, 869–932; b) W. Xia, A. Mahmood, R. Zou, Q. Xu, *Energ. Environ. Sci.* **2015**, *8*, 1837–1866; c) Y. Zhang, S. Yuan, X. Feng, H. Li, J. Zhou, B. Wang, *J. Am. Chem. Soc.* **2016**, *138*, 5785–5788; d) W. Zhang, B. Zheng, W. Shi, X. Chen, Z. Xu, S. Li, Y. R. Chi, Y. Yang, J. Lu, W. Huang, F. Huo, *Adv. Mater.* **2018**, *30*, 1800643.
- [5] M. J. Van Vleet, T. Weng, X. Li, J. R. Schmidt, *Chem. Rev.* **2018**, *118*, 3681–3721.
- [6] Y. Chen, X. Huang, S. Zhang, S. Li, S. Cao, X. Pei, J. Zhou, X. Feng, B. Wang, *J. Am. Chem. Soc.* **2016**, *138*, 10810–10813.
- [7] T. Kitao, Y. Zhang, S. Kitagawa, B. Wang, T. Uemura, *Chem. Soc. Rev.* **2017**, *46*, 3108–3133.
- [8] a) S. Hermes, F. Schröder, R. Chelmoski, C. Wöll, R. A. Fischer, *J. Am. Chem. Soc.* **2005**, *127*, 13744–13745; b) O. Shekhah, H. Wang, M. Paradinas, C. Ocal, B. Schüpbach, A. Terfort, D. Zacher, R. A. Fischer, C. Wöll, *Nat. Mater.* **2009**, *8*, 481–484; c) O. Shekhah, J. Liu, R. A. Fischer, C. Wöll, *Chem. Soc. Rev.* **2011**, *40*, 1081–1106.
- [9] a) X. Huang, B. Zheng, Z. Liu, C. Tan, J. Liu, B. Chen, H. Li, J. Chen, X. Zhang, Z. Fan, W. Zhang, Z. Guo, F. Huo, Y. Yang, L.-H. Xie, W. Huang, H. Zhang, *ACS Nano* **2014**, *8*, 8695–8701; b) P. Falcaro, K. Okada, T. Hara, K. Ikigaki, Y. Tokudome, A. W. Thornton, A. J. Hill, T. Williams, C. Doonan, M. Takahashi, *Nat. Mater.* **2017**, *16*, 342–348; c) R. C. Arbulu, Y.-B. Jiang, E. J. Peterson, Y. Qin, *Angew. Chem. Int. Ed.* **2018**, *57*, 5813–5817; *Angew. Chem.* **2018**, *130*, 5915–5919.
- [10] a) S. Li, J. Huang, *Adv. Mater.* **2016**, *28*, 1143–1158; b) G. Nyström, A. Razaq, M. Strømme, L. Nyholm, A. Mihranyan, *Nano Lett.* **2009**, *9*, 3635–3639; c) Z. Li, C. Yao, Y. Yu, Z. Cai, X. Wang, *Adv. Mater.* **2014**, *26*, 2262–2267.
- [11] a) J. Park, M. Oh, *Nanoscale* **2017**, *9*, 12850–12854; b) H. Zhu, X. Yang, E. D. Cranston, S. Zhu, *Adv. Mater.* **2016**, *28*, 7652–7657; c) M. Matsumoto, T. Kitaoka, *Adv. Mater.* **2016**, *28*, 1765–1769; d) L. Zhu, L. Zong, X. Wu, M. Li, H. Wang, J. You, C. Li, *ACS Nano* **2018**, *12*, 4462–4468; e) J. L. Zhuang, D. Ar, X. J. Yu, J. X. Liu, A. Terfort, *Adv. Mater.* **2013**, *25*, 4631–4635; f) X. Wang, Y. Zheng, T. Wang, X. Xiong, X. Fang, Z. Zhang, *Anal. Methods* **2016**, *8*, 8004–8014; g) E. Zanchetta, L. Malfatti, R. Ricco, M. J. Styles, F. Lisi, C. J. Coghlan, C. J. Doonan, A. J. Hill, G. Brusatin, P. Falcaro, *Chem. Mater.* **2015**, *27*, 690–699.
- [12] a) T. Loiseau, C. Serre, C. Huguenard, G. Fink, F. Taulelle, M. Henry, T. Baille, G. Férey, *Chem. Eur. J.* **2004**, *10*, 1373–1382; b) D. J. Tranchemontagne, J. R. Hunt, O. M. Yaghi, *Tetrahedron* **2008**, *64*, 8553–8557; c) S. A. Basnayake, J. Su, X. Zou, K. J. Balkus, Jr., *Inorg. Chem.* **2015**, *54*, 1816–1821; d) M. Sánchez-Sánchez, N. Getachew, K. Díaz, M. Díaz-García, Y. Chebude, I. Díaz, *Green Chem.* **2015**, *17*, 1500–1509.
- [13] a) G. Lu, S. Li, Z. Guo, O. K. Farha, B. G. Hauser, X. Qi, Y. Wang, X. Wang, S. Han, X. Liu, J. S. DuChene, H. Zhang, Q. Zhang, X. Chen, J. Ma, S. C. Joachim Loo, W. D. Wei, Y. Yang, J. T. Hupp, F. Huo, *Nat. Chem.* **2012**, *4*, 310–316; b) J. T. Yoo, S. H. Lee, C. K. Lee, C. R. Kim, T. Fujigaya, H. J. Park, N. Nakashima, J. K. Shim, *RSC Adv.* **2014**, *4*, 49614–49619; c) H.-X. Zhong, J. Wang, Y.-W. Zhang, W.-L. Xu, W. Xing, D. Xu, Y.-F. Zhang, X.-B. Zhang, *Angew. Chem. Int. Ed.* **2014**, *53*, 14235–14239; *Angew. Chem.* **2014**, *126*, 14459–14463.
- [14] C. Lu, D. Wang, J. Zhao, S. Han, W. Chen, *Adv. Funct. Mater.* **2017**, *27*, 1606219.
- [15] A. Mihranyan, A. Strømme, *Chem. Phys. Lett.* **2004**, *393*, 389–392.
- [16] Y. Kobayashi, T. Saito, A. Isogai, *Angew. Chem. Int. Ed.* **2014**, *53*, 10394–10397; *Angew. Chem.* **2014**, *126*, 10562–10565.
- [17] W. Li, C. Ni, H. Lin, C. P. Huang, S. Ismat Shah, *J. Appl. Phys.* **2004**, *96*, 6663–6668.
- [18] A. J. Howarth, Y. Liu, P. Li, Z. Li, T. C. Wang, J. T. Hupp, O. K. Farha, *Nat. Rev. Mater.* **2016**, *1*, 15018.
- [19] P. G. Yot, Z. Boudene, J. Macia, D. Granier, L. Vanduyfhuys, T. Verstraelen, V. Van Speybroeck, T. Devic, C. Serre, G. Férey, N. Stock, G. Maurin, *Chem. Commun.* **2014**, *50*, 9462–9464.
- [20] a) N. A. Khan, Z. Hasan, S. H. Jhung, *J. Hazard. Mater.* **2013**, *244*, 444–456; b) L. H. Xie, X. M. Liu, T. He, J. R. Li, *Chem* **2018**, *4*, 1911–1927; c) C. Duan, F. Li, M. Yang, H. Zhang, Y. Wu, H. Xi, *Ind. Eng. Chem. Res.* **2018**, *57*, 15385–15394.

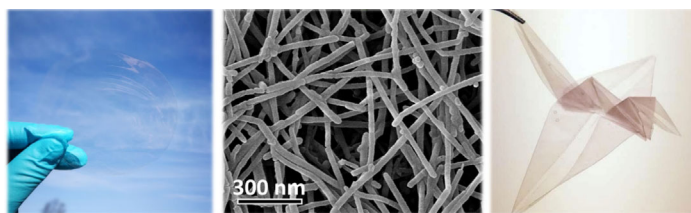
Manuscript received: December 27, 2018

Revised manuscript received: January 17, 2019

Accepted manuscript online: January 28, 2019

Version of record online: ■■■■■ 0000

## COMMUNICATION



**Freestanding nanopapers** are herein fabricated for the first time by the assembly of metal–organic frameworks wrapping on cellulose nanofibers (see figure). The nanopapers exhibit hierarchical meso- and micropores, high op-

tical transparency, excellent mechanical strength, flexibility, and high thermal stability. They may find use as efficient filters for separating volatile organic compounds.

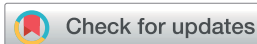
## Nanotechnology

S. Zhou, M. Strømme,\* C. Xu\*



**Highly Transparent, Flexible, and Mechanically Strong Nanopapers of Cellulose Nanofibers @Metal–Organic Frameworks**



Cite this: *J. Mater. Chem. A*, 2018, 6, 24050Received 21st October 2018  
Accepted 9th November 2018

DOI: 10.1039/c8ta10133g

rsc.li/materials-a

# Interweaving metal–organic framework-templated Co–Ni layered double hydroxide nanocages with nanocellulose and carbon nanotubes to make flexible and foldable electrodes for energy storage devices†

Chao Xu,<sup>†</sup> Xueying Kong,<sup>†,ab</sup> Shengyang Zhou,<sup>b</sup> Bing Zheng,<sup>\*a</sup> Fengwei Huo<sup>†,a</sup> and Maria Strømme<sup>\*b</sup>

Metal–organic frameworks (MOFs) and nanocellulose represent emerging and traditional porous materials, respectively. The combination of these two materials in specific ways could generate novel nanomaterials with integrated advantages and versatile functionalities. This study outlines the development of hierarchical porous and conductive nanosheets based on zeolitic imidazolate framework-67 (ZIF-67, a Co-based MOF)-templated Co–Ni layered double hydroxide (LDH) nanocages, *Cladophora* cellulose (CC) nanofibers, and multi-walled carbon nanotubes (CNTs). The LDH–CC–CNT nanosheets can be used as flexible and foldable electrodes for energy storage devices (ESDs). The electrodes are associated with a high areal capacitance of up to 1979 mF cm<sup>-2</sup> at a potential scan rate of 1 mV s<sup>-1</sup>. A flexible, foldable, and hybrid ESD is assembled from LDH–CC–CNT and CC–CNT electrodes with a PVA/KOH gel. The entire device has an areal capacitance of 168 mF cm<sup>-2</sup> and an energy density of 0.6 mW h cm<sup>-3</sup> (60 μW h cm<sup>-2</sup>), at a power density of 8.0 mW cm<sup>-3</sup> (0.8 mW cm<sup>-2</sup>). These promising results demonstrate the potential of using MOFs and sustainable cellulose in flexible, foldable electronic energy storage devices.

## Introduction

There is currently great interest in the development of high performance, thin, flexible, lightweight, environmentally friendly energy storage devices (ESDs).<sup>1–7</sup> Supercapacitors (SCs) constitute an important class of electric energy storage systems that bridges the gap between conventional capacitors and

batteries. Generally, SCs are classified as electrical double layer capacitors (EDLCs) and pseudocapacitors, depending on the charge storage mechanism and the active materials used.<sup>8</sup> EDLCs store charges on the large internal surfaces of active materials such as activated carbon, carbon nanotubes (CNTs) and graphene.<sup>9</sup> Pseudocapacitors rely on electrochemically active materials including certain transition metal oxides, hydroxides, and conducting polymers, for example, RuO<sub>2</sub>,<sup>10</sup> MnO<sub>2</sub>,<sup>11</sup> and polypyrrole,<sup>12</sup> which store electrochemical energy faradaically *via* reversible redox reactions at the interface of the electrode and electrolyte and thus provide higher specific capacitances than EDLCs. In order to increase the energy density, two electrodes with different charge storage behaviours may be applied in the assembly of ESDs.<sup>13,14</sup> For example, asymmetric supercapacitors pair one pseudocapacitive electrode and one capacitive electrode, *e.g.*, MnO<sub>2</sub> and activated carbon.<sup>15</sup> Hybrid capacitors combine faradaic battery-type electrodes and capacitive electrodes, such as Ni(OH)<sub>2</sub> and activated carbon.<sup>16</sup> Because of their high power density, rapid charge/discharge rate, and long operational lifetime, a significant amount of effort has been devoted to the development of flexible SCs and hybrid devices to meet the growing demands of flexible electronics, for instance, foldable phones, roll-up displays, and wearable devices.<sup>17–19</sup>

Metal–organic frameworks (MOFs) are a newly emerging family of functional materials with exceptionally high surface areas and well-defined pores that are constructed by coordination between metal ions or clusters and organic linkers.<sup>20,21</sup> In addition to their well-studied applications in gas storage and separation,<sup>22</sup> catalysis,<sup>23</sup> drug delivery,<sup>24</sup> and sensors,<sup>25</sup> extensive research interest in MOFs has recently been triggered for the exploration of novel electrode materials for SCs.<sup>26–28</sup> Their ordered structures and high surface areas result in fast diffusion of the electrolyte in microporous or mesoporous channels. In addition, transition metal ions or clusters in some MOFs are redox-active centers that can deliver electrochemical activity. Various pristine MOFs and MOF-derived materials have already

<sup>a</sup>Key Laboratory of Flexible Electronics (KLOFE), Institute of Advanced Materials (IAM), Nanjing Tech University (Nanjing Tech), 30 South Puzhu Road, Nanjing 211800, China. E-mail: chao.xu@angstrom.uu.se; iambzheng@njtech.edu.cn

<sup>b</sup>Division of Nanotechnology and Functional Materials, Department of Engineering Sciences, Uppsala University, Uppsala SE-75121, Sweden. E-mail: maria.stromme@angstrom.uu.se

† Electronic supplementary information (ESI) available. See DOI: 10.1039/c8ta10133g

‡ These authors contributed equally to this work.



been successfully applied as capacitive, pseudocapacitive and battery-type electrode materials for ESDs.<sup>29–40</sup> In addition to the conventional considerations for ESDs (*e.g.*, high capacitance, high power density, and long lifetime), flexibility and areal capacitance are more important for flexible ESDs. Recently, a number of MOF-related materials have been fabricated as flexible electrodes for ESDs; these materials are normally coated onto or grown *in situ* on flexible substrates such as plastics, textiles or carbon cloths.<sup>36,41,42</sup> However, the challenge of developing a MOF-related electrode with good flexibility and high areal capacitance for the fabrication of flexible ESDs remains.

Cellulose is the main component of plants and the most naturally abundant biopolymer on earth. Its characteristics of intrinsic flexibility, high mechanical strength, rich organic functional groups, and sustainability make cellulose a promising substrate for the development of novel electrodes.<sup>43,44</sup> More importantly, cellulose can also act as an intrinsic electrolyte reservoir due to its hydrophilic features and ability to swell in water.<sup>45</sup> The hierarchical porous structure formed by cross-linking of cellulose fibers can be used to transfer the electrolyte and diffuse ions in the electrolyte to electrochemically active materials. Because of the versatile functionalities and superior properties of MOFs and cellulose, fabrication of hybrid materials based on MOFs and cellulose could combine the advantages of both materials and allow the design of novel functional materials. However, very few examples of such hybrid materials have been reported to date and the study of their applications has historically been focused only on separations (*e.g.* gas separation and removal of heavy metal ions and dye molecules from polluted aqueous solutions).<sup>46–49</sup> We envision loading MOFs or MOF-related nanocrystals into a flexible cellulose substrate as a feasible approach for the design of novel flexible electrodes with promising electrochemical performance characteristics.

In this paper, we introduce an assembly approach for interweaving nanocellulose fibers, multi-walled carbon nanotubes (CNTs), and ZIF-67 (a cobalt-based zeolitic imidazolate framework, *i.e.* a MOF) nanocrystals into a flexible sheet. A subsequent chemical etching process converts the loaded MOF nanocrystals into Co–Ni layered double hydroxide (LDH) nanocages with unique hollow structures, a well-known electrochemically active material.<sup>50–52</sup> This strategy involves the formation of a flexible, conductive substrate and the subsequent interweaving of the isolated LDH nanocages with nanocellulose and CNTs. The nanocellulose enables the knitting process and reinforces the LDH nanocages on the substrate, while also providing the flexibility of the composite, and the CNTs act as conductive bridges for electron transfer between the LDH nanocages. The resultant flexible and conductive composite containing compactly interconnected and homogeneously dispersed nanostructures can be used as a high performance electrode for the assembly of flexible and foldable ESDs.

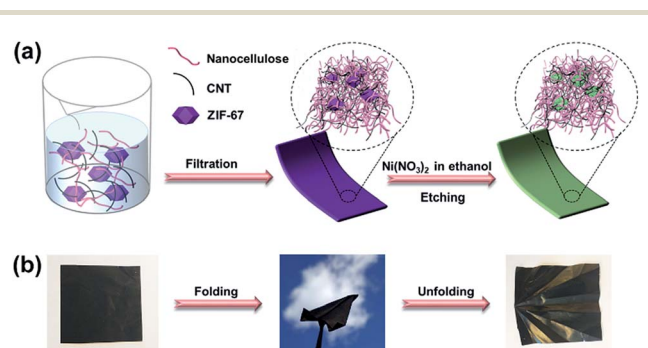
## Results and discussion

*Cladophora* cellulose (CC), a type of nanofibrillated cellulose extracted from an environmentally polluting green alga, was

chosen as the substrate in this study. Firstly, it was expected that MOF nanocrystals could be loaded into its nanofibrous and mesoporous structure.<sup>53,54</sup> Moreover, its high crystallinity<sup>55</sup> gives rise to the outstanding mechanical flexibility of the substrate, which is an important characteristic of flexible electronic devices. Scheme 1 illustrates the synthesis procedures. Firstly, the as-synthesized ZIF-67 nanocrystals (pre-dispersed in ethanol), CC, and CNTs, with a mass ratio of 2 : 1 : 3, are dispersed in water by sonication to form a homogeneous mixture. The dispersion is then vacuum filtered using a membrane filter, and the filter cake is dried to form a free-standing composite, called a ZIF–CC–CNT nanosheet. The composite is then immersed in an ethanol solution of nickel nitrate for three hours to etch the ZIF-67 nanocrystals. During this time, the protons generated from the hydrolysis of Ni<sup>2+</sup> ions gradually digest the core structure of the ZIF-67 nanocrystals and release Co<sup>2+</sup> ions into the ethanol solution. The released Co<sup>2+</sup> ions are partly oxidized to Co<sup>3+</sup> by the NO<sub>3</sub><sup>−</sup> ions in the presence of the protons, followed by further co-precipitation of Ni<sup>2+</sup> and Co<sup>2+</sup>/Co<sup>3+</sup> and the formation of Ni–Co LDH shells, templated by ZIF-67 nanocrystals.<sup>56</sup> Finally, a freestanding, flexible, and foldable composite, called an LDH–CC–CNT nanosheet, is obtained.

With the fixed ratio of the three components in the initial dispersions, the thickness and areal density of the active materials in the hybrid nanosheets can be precisely controlled by adjusting the total amounts of the starting materials. Three ZIF–CC–CNT nanosheets and the three corresponding LDH–CC–CNT nanosheets with tuned thicknesses (9, 39, and 103 μm) were prepared. Thermogravimetric analysis (Fig. S1†) indicated that the content of the active material ZIF-67 was 0.305, 0.754, and 1.720 mg cm<sup>−2</sup> in the ZIF–CC–CNT nanosheet and LDH was 0.225, 0.481, and 1.452 mg cm<sup>−2</sup> in the LDH–CC–CNT nanosheet.

The structures of the ZIF–CC–CNT and LDH–CC–CNT nanosheets were fully characterized by powder X-ray diffraction (XRD), X-ray photoelectron spectroscopy (XPS), and X-ray energy dispersive spectroscopy (EDS). The XRD pattern of ZIF–CC–CNT in Fig. 1a clearly shows the existence of ZIF-67, cellulose and



**Scheme 1** (a) Schematic illustration of the formation process of LDH–CC–CNT nanosheets; (b) optical images of a flexible, foldable LDH–CC–CNT nanosheet (size: 4 cm × 4 cm). CC = *Cladophora* cellulose; LDH = Co–Ni layered double hydroxide nanocages; CNTs = carbon nanotubes.



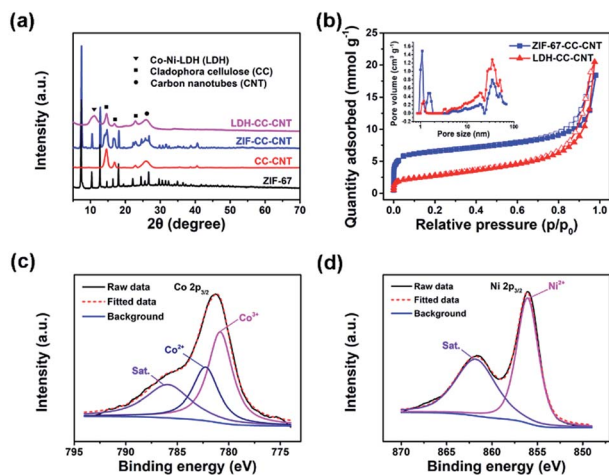


**Fig. 1** (a) A comparison of powder X-ray diffraction patterns of pure ZIF-67, *Cladophora* cellulose (CC)-CNTs, ZIF-CC-CNT nanosheets, and LDH-CC-CNT nanosheets; (b) N<sub>2</sub> adsorption and desorption isotherms of ZIF-CC-CNT and LDH-CC-CNT nanosheets, recorded at 77 K. The inset shows the pore size distributions calculated from the adsorption branches using density functional theory; (c) high-resolution Co 2p<sub>3/2</sub> and (d) Ni 2p<sub>3/2</sub> X-ray photoelectron spectra of LDH-CC-CNT. CNT = carbon nanotube; LDH = Co-Ni layered double hydroxide nanocages.

CNTs, thus confirming the composition of the nanosheet. The diffraction peaks for ZIF-67 were entirely absent after etching the composite in an ethanol solution of Ni(NO<sub>3</sub>)<sub>2</sub>·6H<sub>2</sub>O, and the peaks for a typical LDH structure were found, confirming the formation of an LDH structure by the reaction between ZIF-67 and Ni(NO<sub>3</sub>)<sub>2</sub>·6H<sub>2</sub>O (Fig. 1a and S2†). Strong and narrow diffraction peaks at  $2\theta = 14, 17$  and  $22^\circ$  in both the ZIF-CC-CNT and the LDH-CC-CNT nanosheets confirmed the high crystallinity of the CC nanofibers.<sup>57</sup> The elemental composition of LDH-CC-CNT was confirmed by EDS and XPS studies. The EDS spectrum of the selected area of LDH-CC-CNT (Fig. S3†) revealed that the LDH nanocages contained Co and Ni, with a Co : Ni ratio of 1 : 2.1. The XPS survey scan spectrum of LDH-CC-CNT (Fig. S4†) indicated the presence of C, O, N, Ni, and Co in the composite. Fig. 1c and d show the high resolution XPS spectra of LDH-CC-CNT in the Co 2p<sub>3/2</sub> and Ni 2p<sub>3/2</sub> regions. The deconvoluted peaks at 782.3 and 780.8 eV in the Co 2p<sub>3/2</sub> spectrum correspond to Co<sup>2+</sup> and Co<sup>3+</sup>, respectively,<sup>58</sup> confirming that a portion of the Co<sup>2+</sup> ions released from ZIF-67 were oxidized to Co<sup>3+</sup> during the etching procedure. The single peak located at 856.1 eV in the Ni 2p<sub>3/2</sub> spectrum indicated the existence of Ni<sup>2+</sup> in the LDH structure.<sup>59</sup>

Nitrogen sorption measurements at 77 K were carried out to analyze the porosity of the samples. As shown in Fig. 1b, the adsorption isotherm for ZIF-CC-CNT, with rapid N<sub>2</sub> uptake at low partial pressures ( $P/P_0 < 0.1$ ), revealed the microporous structure of ZIF-67. Meanwhile, the pore size distribution analysis based on the adsorption isotherm indicated that ZIF-CC-CNT had relatively narrow micropores, with pore sizes centered at 1.0 and 1.4 nm, whereas these typical micropores were absent in LDH-CC-CNT because of the digestion of the framework of ZIF-67 during the etching procedure. Accordingly,

the calculated Brunauer–Emmett–Teller (BET) surface areas for LDH-CC-CNT of different thicknesses lie in the range of 219 to 261 m<sup>2</sup> g<sup>-1</sup>; these were significantly smaller than those for ZIF-CC-CNT (525–693 m<sup>2</sup> g<sup>-1</sup>). The size of the micropores in LDH-CC-CNT (1.2 nm) can be attributed to the presence of CNTs (Fig. S5†). Both ZIF-CC-CNT and LDH-CC-CNT samples showed mesoporous structures generated by interweaving CC nanofibers and CNTs with pore size distributions in the range of 20.0 to 34.4 nm.

The morphology of the ZIF-CC-CNT and LDH-CC-CNT nanosheets was studied by field emission scanning electron microscopy (FESEM) to reveal the interconnections between the ZIF-67 or LDH nanocrystals, the CC nanofibers, and the CNTs. The as-synthesized ZIF-67 nanocrystals had a typical rhombic dodecahedral morphology and an average size of approximately 800 nm (Fig. S6a†). SEM images (Fig. 2) revealed the surface morphology of the ZIF-CC-CNT and LDH-CC-CNT nanosheets at different magnifications. The cross-linked CC nanofibers and CNTs (with diameters of about 30 nm and 10 nm, respectively) were interwoven in the well-dispersed ZIF-67 crystals to form the framework of the ZIF-CC-CNT nanosheets. More importantly, the ZIF-67 nanocrystals were not only attached to the surface of the nanosheets but were also entangled in the matrix, as indicated by the “bumps” in the SEM images, suggesting that ZIF-67 nanocrystals were evenly distributed throughout the entire nanosheet. In comparison, in the ZIF-CNT composite, the ZIF-67 nanocrystals formed agglomerates with the CNTs, which remained separate in the absence of cellulose nanofibers (Fig. S6b and c†). Therefore, we can conclude that CC nanofibers play a key role in the formation of uniform and intimately connected nanostructures because of their ability to aid in the dispersion and intertwining of the active materials.

After etching the ZIF-CC-CNT nanosheets in a solution of Ni(NO<sub>3</sub>)<sub>2</sub>·6H<sub>2</sub>O in ethanol, where the ZIF-67 nanocrystals were transformed into hollow LDH nanocages, these uniform and interconnected nanostructures were successfully transformed into LDH-CC-CNT nanosheets. It was expected that the uniformity of the LDH-CC-CNT nanosheets and the hollow nanostructure of LDH would lead to fully accessible sites for the active materials and fast diffusion of guest molecules or ions. Furthermore, the intimate connections between the LDH nanocages and the flexible and conductive matrix composed of nanocellulose and CNTs could effectively improve the conductivity of LDH. Considering the flexible, binder-free, conductive, and fully accessible characteristics of these structures, we anticipated that LDH-CC-CNT nanosheets would make effective electrode materials.

The electrochemical performance of the LDH-CC-CNT electrodes was studied in a traditional three-electrode cell using 1.0 M aqueous KOH as the electrolyte. Binder-free electrodes were prepared by pressing a piece of LDH-CC-CNT nanosheet (1 × 2 cm) at a pressure of 150 MPa onto a piece of flexible graphite paper as the current collector. The design of these binder-free electrodes was chosen to avoid “dead” mass and volume in the electrode, thus increasing its gravimetric/volumetric capacity. Fig. 3a shows the cyclic voltammetry (CV) curves of the LDH-CC-CNT (9 μm, 0.225 mg cm<sup>-2</sup> LDH)



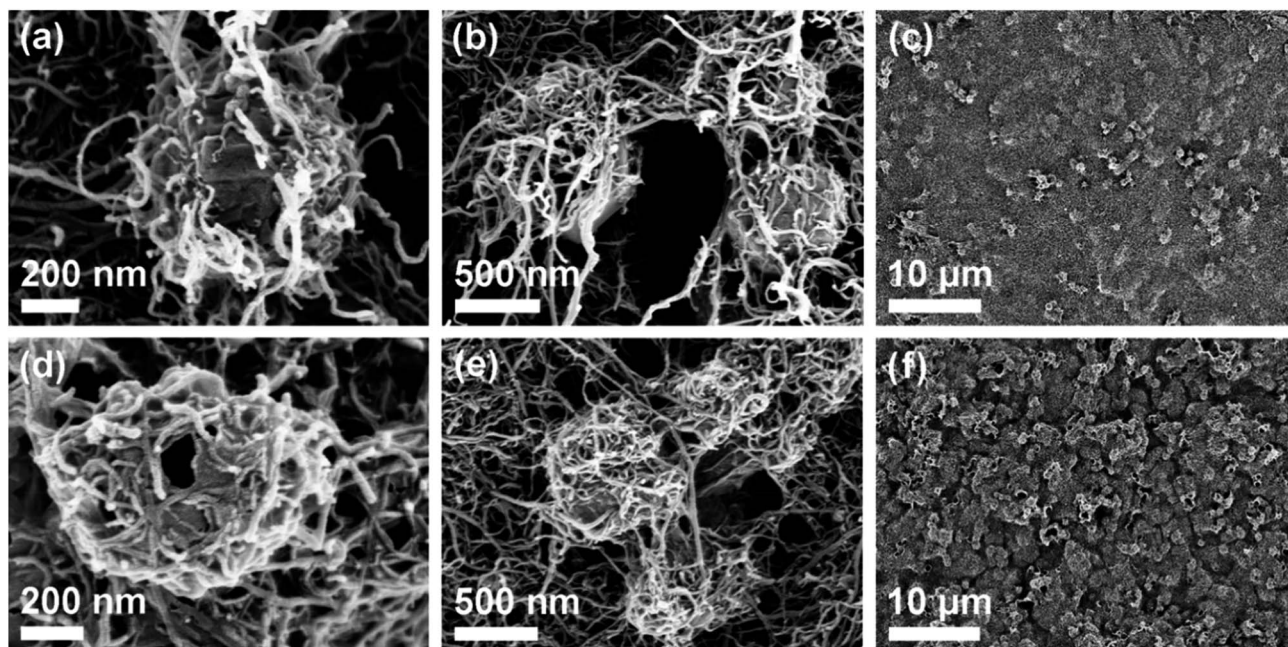


Fig. 2 Scanning electron microscopy images of (a–c) ZIF-CC-CNT and (d–f) LDH-CC-CNT nanosheets at different magnifications. CC = *Cladophora* cellulose; CNT = carbon nanotube; LDH = Co–Ni layered double hydroxide nanocages.

electrode at different scan rates ( $1\text{--}30\text{ mV s}^{-1}$ ) in the potential range of 0 to 0.6 V vs. Hg/HgO. With the increasing scan rate from 1 to 30 mV, the CV curves were similar in shape, with slightly shifted peak positions. The CV curve at a scan rate of

$1\text{ mV s}^{-1}$  had a distinct pair of redox peaks at 0.40 and 0.29 V vs. Hg/HgO, related to the electrochemical redox reactions of  $\text{Ni}(\text{OH})_2/\text{NiOOH}$  and  $\text{CoOOH}/\text{CoO}_2$  in LDH.<sup>50</sup> It should be noted that it is difficult to distinguish redox peaks for these two

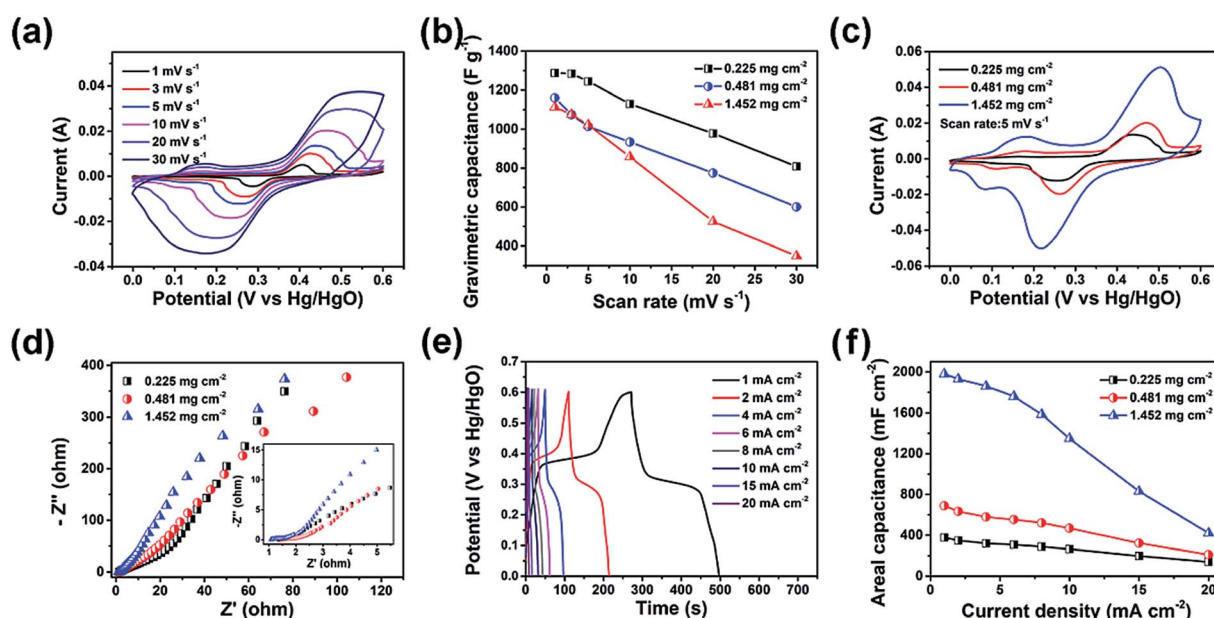
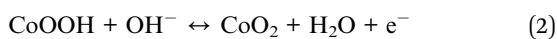


Fig. 3 (a) Cyclic voltammetry (CV) curves of LDH-CC-CNT with a mass loading of  $0.225\text{ mg cm}^{-2}$  LDH at different scan rates. (b) Gravimetric capacitance and rate performance of LDH in the LDH-CC-CNT electrodes with different areal densities (values on the vertical axis are normalized with respect to the LDH content of the electrode). (c) CV curves of LDH-CC-CNT with different mass loadings of LDH at a scan rate of  $5\text{ mV s}^{-1}$ . (d) Nyquist plots of LDH-CC-CNT electrodes; the inset shows a close-up of the high frequency data. (e) Galvanostatic charge-discharge (GCD) curves of an LDH-CC-CNT electrode ( $0.225\text{ mg cm}^{-2}$  LDH). (f) Areal capacitance and rate performance of LDH-CC-CNT electrodes with different areal densities. CC = *Cladophora* cellulose; CNT = carbon nanotube; LDH = Co–Ni layered double hydroxide nanocages.



reactions because of the similar redox potentials for  $\text{Ni}^{2+}/\text{Ni}^{3+}$  and  $\text{Co}^{3+}/\text{Co}^{4+}$ .<sup>56</sup> In addition, a pair of broad and inconspicuous redox peaks in the potential range of 0.1 to 0.2 V vs. Hg/HgO was observed in the CV curve. This pair of redox peaks at low potentials can be ascribed to the redox reaction of  $\text{Co}(\text{OH})_2/\text{CoOOH}$  and further confirms the existence of  $\text{Co}^{2+}$  in the LDH structure.<sup>59</sup> Based on this analysis of the CV curves, we hypothesized that the electrochemical reaction process in the LDH is as follows:



In order to investigate the charge storage mechanism of the LDH-CC-CNT electrodes, we studied the voltammetric response at various scan rates in the CV measurements. In principle, the dependence of the peak current ( $i_p$ ) on the scan rate ( $\nu$ ) can be expressed as<sup>8,13</sup>

$$i_p = a\nu^b \quad (4)$$

where  $a$  and  $b$  are adjustable parameters.

Generally, the peak current is proportional to the square root of the scan rate ( $b = 0.5$ ) for a battery-type faradaic reaction, whereas the pseudocapacitive current is linearly dependent on the scan rate ( $b = 1$ ). We found that the plots of peak current vs. scan rate can be linearly fitted with  $b = 0.5$  for the three electrodes of LDH-CC-CNT with different loadings of LDH (Fig. S7†), suggesting that the LDH-CC-CNT electrodes are battery-type electrodes and the charge storage mechanism is mainly based on the diffusion-controlled intercalation/deintercalation of the electrolyte ions.<sup>59–61</sup>

The capacitances of the active material (LDH) and the entire electrode were calculated by analyzing the CV curves. In order to evaluate the contributions of the CNTs and the current collector to the capacitance of the electrode, a background electrode composed of CC and CNTs on graphite paper was prepared for electrochemical analysis. Based on the CV curves of LDH-CC-CNT and this CC-CNT electrode at  $1 \text{ mV s}^{-1}$  and by deducting the contributions of the CNTs and graphite paper, the specific capacitance of LDH was calculated to be  $1287.8 \text{ F g}^{-1}$ , which is comparable to the reported values for Co-Ni LDH.<sup>50,51,62–64</sup> Importantly, the gravimetric capacitance of LDH was not significantly reduced in the electrode with a higher mass loading, as shown in Fig. 3b. In contrast, the capacitance of LDH was only  $732.2 \text{ F g}^{-1}$  in an LDH-PVDF-CNT electrode prepared by coating LDH, CNTs and a binder of polyvinylidene fluoride (PVDF) on graphite paper in a traditional manner, under the same conditions (Fig. S8†). Comparison of the nanostructures in the SEM images provides a possible explanation for this large difference in the capacitive performance of LDH in the two electrodes. As mentioned above, the LDH nanocages were uniformly dispersed and interconnected by cellulose nanofibers and CNTs in the LDH-CC-CNT nanosheets. In contrast, the LDH-PVDF-CNT electrode displayed

agglomerates of LDH nanocages attached onto the surface of the CNT matrix (Fig. S6d and e†). Consequently, the rates of ion diffusion and electron transfer were limited, leading to the much lower capacitance. These results strongly supported our assumption that the electrochemical performance of the electrode could be significantly increased by forming a uniform and interwoven nanostructure within the conductive substrate.

For flexible and wearable electronic devices, areal capacitance is even more important than gravimetric capacitance. In general, the areal capacitance of an electrode increases with the increasing areal density of the active material in the substrate. However, aggregation and stacking of the active materials usually occur with subsequently increased resistance.<sup>65</sup> As a result, the areal capacitance will gradually reach a plateau when the mass loading is increased, and the electrochemical performance of the active material will be much lower than the theoretical value. In order to evaluate the effects of mass loading and thickness on the electrochemical performance, LDH-CC-CNT electrodes with different mass loadings (0.225, 0.481, and  $1.452 \text{ mg cm}^{-2}$  LDH) and thicknesses (9, 39, and  $103 \mu\text{m}$ ) were studied using CV (Fig. S9†). Fig. 3c shows a comparison of the CV curves of the three electrodes at the same scan rate of  $5 \text{ mV s}^{-1}$ . Notably, the redox peak positions only shifted slightly with the increasing thickness and mass loading. Meanwhile, the electrochemical impedance spectroscopy (EIS) results displayed as Nyquist plots in Fig. 3d revealed that both the high frequency resistance and the charge transfer resistance for LDH-CC-CNT electrodes were relatively low, and these resistances were not significantly affected by increasing the mass loading and thickness because of the uniform nanostructure of the conductive electrodes.

Galvanostatic charge-discharge (GCD) measurements were performed to evaluate the energy storage performance of the LDH-CC-CNT electrodes (Fig. S10†). The highly symmetrical shape of the chronopotentiometric curves reflected the reversible redox reactions in the electrode (Fig. 3e). The discharge curves showed that the areal capacitances of the LDH-CC-CNT electrodes with mass loadings of 0.225, 0.481, and  $1.452 \text{ mg cm}^{-2}$  LDH were  $377.5$ ,  $688.6$  and  $1979.2 \text{ mF cm}^{-2}$ , respectively, at a current density of  $1 \text{ mA cm}^{-2}$ . The three electrodes retained 37.1, 30.5, and 21.2% of their capacitances when the current density was increased from 1 to  $20 \text{ mA cm}^{-2}$ , indicating a good rate capability (Fig. 3f). Importantly, the flexibility of the electrode was not influenced by increasing the thickness and mass loading towards higher areal capacitances. A further increase in the mass loading of LDH to  $2.87 \text{ mg cm}^{-2}$  in the LDH-CC-CNT nanosheet with a thickness of  $212 \mu\text{m}$  achieved an even higher areal capacitance of  $3200 \text{ mF cm}^{-2}$ ; however, the electrode had a very poor rate capability and was not as flexible. Nonetheless, the value of  $1979.2 \text{ mF cm}^{-2}$  for the areal capacitance of the LDH-CC-CNT electrode ranks as one of the highest reported for LDH-based electrodes (Co-Ni LDH/carbon fiber paper:<sup>66</sup>  $1640 \text{ mF cm}^{-2}$  at  $2 \text{ mA cm}^{-2}$ ;  $\text{NiCo}_2\text{S}_4$ @Ni-Mn LDH/graphene sponge:<sup>67</sup>  $1740 \text{ mF cm}^{-2}$  at  $1 \text{ mA cm}^{-2}$ ; Ni-Co@Ni-Co LDH nanotube array/carbon fiber cloth:<sup>62</sup>  $2000 \text{ mF cm}^{-2}$  at  $4.6 \text{ mA cm}^{-2}$ ; NiCo-LDH/carbon fiber cloth:<sup>59</sup>  $2242 \text{ mF cm}^{-2}$  at  $1 \text{ mA cm}^{-2}$ ).



To demonstrate the potential of the composite electrode for practical applications in flexible electronics, we assembled a flexible, foldable, and all-solid-state hybrid ESD. As shown in Fig. 4a, the LDH-CC-CNT (1 cm × 2 cm, 0.481 mg cm<sup>-2</sup> LDH) and CC-CNT (1 cm × 2 cm, 3.375 mg cm<sup>-2</sup> CNTs) nanosheets were used as the positive and negative electrodes, respectively. A poly(vinyl alcohol)/KOH gel was used as the solid electrolyte, and a piece of filter paper (1.2 cm × 2.5 cm) was used as the separator. The total volume of the assembled device was 0.2 cm<sup>3</sup>. The CV curves in Fig. 4b present the potential windows of -1.0 to 0 V vs. Hg/HgO for the LDH-CC-CNT electrode and 0 to 0.6 V vs. Hg/HgO for the CC-CNT electrode at the same scan rate of 5 mV s<sup>-1</sup>. It was anticipated that this hybrid ESD could reach a high operating potential. CV curves of the hybrid ESD were recorded in the two-electrode system at a scan rate of 50 mV s<sup>-1</sup> within the potential window from 0–1 V to 0–1.6 V (vs. Hg/HgO), as shown in Fig. 4c. This demonstrated that the stable operating voltage could be extended to 1.6 V. In addition, CV curves of the hybrid ESD at different scan rates (10–50 mV s<sup>-1</sup>) were measured within the potential window of 0–1.6 V vs. Hg/HgO (Fig. S11†). The almost rectangular shapes of the CV curves at low operating potentials demonstrated the double-layer capacitance of CC-CNT. Broad redox peaks were observed at high operating potentials, indicating a combined contribution of both capacity and double-layer capacitance in the hybrid ESD. To evaluate the flexibility and foldability of the hybrid ESD, we recorded the CV curves when the device was folded to 90° and 180°. As shown in Fig. 4d, the CV curves were only very slightly different before and during folding, indicating that the device was fully flexible and foldable.

The specific capacitance, and energy and power density of the hybrid ESD were calculated from the GCD measurements.

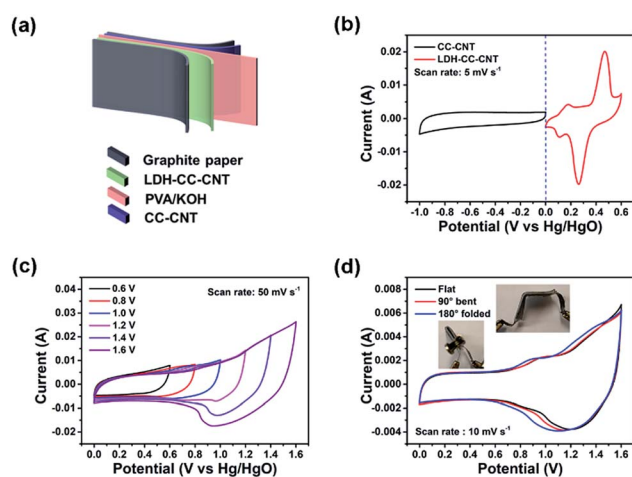


Fig. 4 (a) Schematic illustration of the flexible and solid-state hybrid ESD LDH-CC-CNT//CC-CNT. (b) Cyclic voltammetry (CV) curves of LDH-CC-CNT and CC-CNT electrodes at the same scan rate. (c) CV curves of the device at different potential windows at the same scan rate. (d) CV curves of the device under different bending conditions. ESD = energy storage device; CC = *Cladophora* cellulose; CNT = carbon nanotube; LDH = Co-Ni layered double hydroxide.

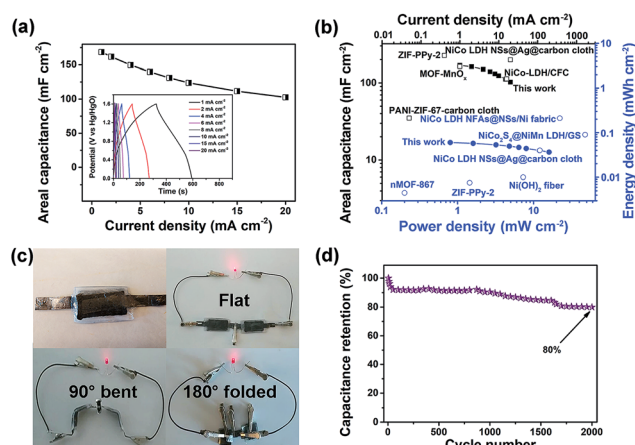


Fig. 5 (a) Galvanostatic charge-discharge curves of the flexible and solid-state hybrid ESD LDH-CC-CNT//CC-CNT and the calculated areal capacitances at different current densities. (b) Comparison of areal capacitance (■ this work, □ reported values), and power and energy density (● this work, ○ reported values) of the device with those of other flexible ESDs based on electrodes of nMOF-867,<sup>29</sup> MOF-MnO<sub>x</sub>,<sup>41</sup> PANI-ZIF-67-carbon cloth,<sup>42</sup> NiCo-LDH/CFC,<sup>59</sup> NiCo<sub>2</sub>S<sub>4</sub>@NiMn-LDH/GS,<sup>67</sup> NiCo-LDH NSs@Ag@carbon cloth,<sup>68</sup> NiCo-LDH NFAs@NSs/Ni fabric,<sup>69</sup> ZIF-PPy-2,<sup>70</sup> Ni(OH)<sub>2</sub> nanofibers<sup>71</sup> and various carbon electrodes. (c) Photo of red LEDs powered by the bent or folded device. (d) Cycling performance of the device. ESD = energy storage device; CC = *Cladophora* cellulose; CNT = carbon nanotube; LDH = layered double hydroxide; PANI = polyaniline; PPy = polypyrrole; CFC = carbon fiber cloth; NFAs = nanoflake arrays; NSs = nanosheets; GS = graphene sponge.

The areal capacitance for the whole cell was 168.3, 149.5, 123.8, and 102.5 mF cm<sup>-2</sup> at discharge current densities of 1, 4, 10, and 20 mA cm<sup>-2</sup>, respectively (Fig. 5a). Accordingly, the maximum energy and power densities of the hybrid ESD were 0.6 mW h cm<sup>-3</sup> (60 μW h cm<sup>-2</sup>) and 160 mW cm<sup>-3</sup> (16 mW cm<sup>-2</sup>), respectively (Fig. 5b). The values of areal capacitance, and energy and power density were comparable to those for state-of-the-art flexible SCs (Table S1†).<sup>29,67–71</sup> It should be noted that the volume of the whole hybrid ESD was considered when calculating the volumetric energy/power densities. We also assembled two hybrid ESD units in series to power an LED. As seen in Fig. 5c, the devices in the series light the LED even when they were folded. The long-term stability of the hybrid ESD was tested through continuous CV cycling. As shown in Fig. 5d, the hybrid device retained more than 80% of its original capacitance after 2000 cycles at 50 mV s<sup>-1</sup>. Collectively, the electrochemical studies suggested that the all-solid-state hybrid ESD showed an excellent capacitive behavior, a good rate capability, and excellent flexibility and foldability.

## Conclusions

In conclusion, novel LDH-CC-CNT nanosheets have been successfully prepared by interweaving MOF-derived Co-Ni LDH nanocages with CC nanofibers and CNTs. The electrodes based on LDH-CC-CNT nanosheets had a very high areal capacitance and a good rate capability. Given their excellent flexibility and



foldability, along with their superior electrochemical performance, the LDH-CC-CNT electrodes were fabricated into an all-solid-state hybrid ESD. We conclude that the interwoven, hierarchically porous, fully accessible, and conductive nanostructures in the LDH-CC-CNT nanosheets play a key role in the electrochemical performance of the hybrid ESD. An external current collector is required for this electrode and energy storage device because of the limited interactions between the hydrophobic CNTs, and the hydrophilic nanocellulose and LDH nanocages. This limitation could be overcome by using chemically modified nanocellulose and CNTs in high quality dispersions to design highly compact and conductive matrices.<sup>72</sup> Thus, this study opens up a path for the development of new designs for thin, flexible, lightweight, and high-performance electronic energy storage devices based on MOF-related materials and sustainable cellulose.

## Conflicts of interest

There are no conflicts to declare.

## Acknowledgements

The project was supported by an Åforsk research grant (18-413), a STINT initiation grant (IB2017-6985), the National Natural Science Foundation of China (21504043), and the Natural Science Foundation of Jiangsu Province (BK20170994). We thank Prof. Martin Sjödin and Dr Zhaohui Wang for valuable discussions.

## Notes and references

- V. L. Pushparaj, M. M. Shaijumon, A. Kumar, S. Murugesan, L. Ci, R. Vajtai, R. J. Linhardt, O. Nalamasu and P. M. Ajayan, *Proc. Natl. Acad. Sci. U. S. A.*, 2007, **104**, 13574–13577.
- L. Hu and Y. Cui, *Energy Environ. Sci.*, 2012, **5**, 6423–6435.
- X. Wang, X. Lu, B. Liu, D. Chen, Y. Tong and G. Shen, *Adv. Mater.*, 2014, **26**, 4763–4782.
- H. Wang, Y. Yang and L. Guo, *Adv. Energy Mater.*, 2016, **7**, 1601709.
- G. Nyström, A. Razaq, M. Strømme, L. Nyholm and A. Mihranyan, *Nano Lett.*, 2009, **9**, 3635–3639.
- Z. Wang, P. Tammela, M. Strømme and L. Nyholm, *Adv. Energy Mater.*, 2017, **7**, 1700130.
- Q. Meng, K. Cai, Y. Chen and L. Chen, *Nano Energy*, 2017, **36**, 268–285.
- Y. Wang, Y. Song and Y. Xia, *Chem. Soc. Rev.*, 2016, **45**, 5925–5950.
- L. L. Zhang and X. S. Zhao, *Chem. Soc. Rev.*, 2009, **38**, 2520–2531.
- J. H. Park and O. O. Park, *J. Power Sources*, 2002, **109**, 121–126.
- V. Subramanian, H. Zhu and B. Wei, *J. Power Sources*, 2006, **159**, 361–364.
- T. Liu, L. Finn, M. Yu, H. Wang, T. Zhai, X. Lu, Y. Tong and Y. Li, *Nano Lett.*, 2014, **14**, 2522–2527.
- Y. Shao, M. F. El-Kady, J. Sun, Y. Li, Q. Zhang, M. Zhu, H. Wang, B. Dunn and R. B. Kaner, *Chem. Rev.*, 2018, **118**, 9233–9280.
- N. Choudhary, C. Li, J. Moore, N. Nagaiah, L. Zhai, Y. Jung and J. Thomas, *Adv. Mater.*, 2017, **29**, 1605336.
- T. Brousse, M. Toupin and D. Bélanger, *J. Electrochem. Soc.*, 2004, **151**, A614–A622.
- J. Huang, P. Xu, D. Cao, X. Zhou, S. Yang, Y. Li and G. Wang, *J. Power Sources*, 2014, **246**, 371–376.
- J. Bae, K. Song Min, J. Park Young, M. Kim Jong, M. Liu and Z. L. Wang, *Angew. Chem., Int. Ed.*, 2011, **50**, 1683–1687.
- M. F. El-Kady and R. B. Kaner, *Nat. Commun.*, 2013, **4**, 1475.
- L. Liu, Z. Niu, L. Zhang, W. Zhou, X. Chen and S. Xie, *Adv. Mater.*, 2014, **26**, 4855–4862.
- O. M. Yaghi, M. O'Keeffe, N. W. Ockwig, H. K. Chae, M. Eddaoudi and J. Kim, *Nature*, 2003, **423**, 705–714.
- S. Kitagawa, R. Kitaura and S. i. Noro, *Angew. Chem., Int. Ed.*, 2004, **43**, 2334–2375.
- T. Rodenas, I. Luz, G. Prieto, B. Seoane, H. Miro, A. Corma, F. Kapteijn, F. X. Llabrés i Xamena and J. Gascon, *Nat. Mater.*, 2015, **14**, 48–55.
- W. Zhang, B. Zheng, W. Shi, X. Chen, Z. Xu, S. Li, R. Chi Yonggui, Y. Yang, J. Lu, W. Huang and F. Huo, *Adv. Mater.*, 2018, **30**, 1800643.
- Y. Chen, P. Li, J. A. Modica, R. J. Drouot and O. K. Farha, *J. Am. Chem. Soc.*, 2018, **140**, 5678–5681.
- G. Lu and J. T. Hupp, *J. Am. Chem. Soc.*, 2010, **132**, 7832–7833.
- L. Wang, Y. Han, X. Feng, J. Zhou, P. Qi and B. Wang, *Coord. Chem. Rev.*, 2016, **307**, 361–381.
- X. Cao, C. Tan, M. Sindoro and H. Zhang, *Chem. Soc. Rev.*, 2017, **46**, 2660–2677.
- H. B. Wu and X. W. Lou, *Sci. Adv.*, 2017, **3**, eaap9252.
- K. M. Choi, H. M. Jeong, J. H. Park, Y.-B. Zhang, J. K. Kang and O. M. Yaghi, *ACS Nano*, 2014, **8**, 7451–7457.
- J. Yang, P. Xiong, C. Zheng, H. Qiu and M. Wei, *J. Mater. Chem. A*, 2014, **2**, 16640–16644.
- W. H. Li, K. Ding, H. R. Tian, M. S. Yao, B. Nath, W. H. Deng, Y. Wang and G. Xu, *Adv. Funct. Mater.*, 2017, **27**, 1702067.
- D. Sheberla, J. C. Bachman, J. S. Elias, C.-J. Sun, Y. Shao-Horn and M. Dincă, *Nat. Mater.*, 2016, **16**, 220–224.
- D. Feng, T. Lei, M. R. Lukatskaya, J. Park, Z. Huang, M. Lee, L. Shaw, S. Chen, A. A. Yakovenko, A. Kulkarni, J. Xiao, K. Fredrickson, J. B. Tok, X. Zou, Y. Cui and Z. Bao, *Nat. Energy*, 2018, **3**, 30–36.
- F. Meng, Z. Fang, Z. Li, W. Xu, M. Wang, Y. Liu, J. Zhang, W. Wang, D. Zhao and X. Guo, *J. Mater. Chem. A*, 2013, **1**, 7235–7241.
- R. Bendi, V. Kumar, V. Bhavanasi, K. Parida and S. Lee Pooi, *Adv. Energy Mater.*, 2015, **6**, 1501833.
- C. Guan, X. Liu, W. Ren, X. Li, C. Cheng and J. Wang, *Adv. Energy Mater.*, 2017, **7**, 1602391.
- P. Pachfule, D. Shinde, M. Majumder and Q. Xu, *Nat. Chem.*, 2016, **8**, 718–724.
- R. R. Salunkhe, Y. V. Kaneti, J. Kim, J. H. Kim and Y. Yamauchi, *Acc. Chem. Res.*, 2016, **49**, 2796–2806.



- 39 Q. Liu, X. Liu, C. Shi, Y. Zhang, X. Feng, M.-L. Cheng, S. Su and J. Gu, *Dalton Trans.*, 2015, **44**, 19175–19184.
- 40 X. Liu, C. Shi, C. Zhai, M. Cheng, Q. Liu and G. Wang, *ACS Appl. Mater. Interfaces*, 2016, **8**, 4585–4591.
- 41 Y.-Z. Zhang, T. Cheng, Y. Wang, W.-Y. Lai, H. Pang and W. Huang, *Adv. Mater.*, 2016, **28**, 5242–5248.
- 42 L. Wang, X. Feng, L. Ren, Q. Piao, J. Zhong, Y. Wang, H. Li, Y. Chen and B. Wang, *J. Am. Chem. Soc.*, 2015, **137**, 4920–4923.
- 43 L. Nyholm, G. Nyström, A. Mihranyan and M. Strømme, *Adv. Mater.*, 2011, **23**, 3751–3769.
- 44 M. Hamed, E. Karabulut, A. Marais, A. Herland, G. Nyström and L. Wågberg, *Angew. Chem., Int. Ed.*, 2013, **52**, 12038–12042.
- 45 Z. Gui, H. Zhu, E. Gillette, X. Han, G. W. Rubloff, L. Hu and S. B. Lee, *ACS Nano*, 2013, **7**, 6037–6046.
- 46 M. Matsumoto and T. Kitaoka, *Adv. Mater.*, 2016, **28**, 1765–1769.
- 47 H. Zhu, X. Yang, E. D. Cranston and S. Zhu, *Adv. Mater.*, 2016, **28**, 7652–7657.
- 48 J. Park and M. Oh, *Nanoscale*, 2017, **9**, 12850–12854.
- 49 L. Zhu, L. Zong, X. Wu, M. Li, H. Wang, J. You and C. Li, *ACS Nano*, 2018, **12**, 4462–4468.
- 50 Z. Jiang, Z. Li, Z. Qin, H. Sun, X. Jiao and D. Chen, *Nanoscale*, 2013, **5**, 11770–11775.
- 51 G. Nagaraju, G. S. R. Raju, Y. H. Ko and J. S. Yu, *Nanoscale*, 2016, **8**, 812–825.
- 52 X. Li, D. Du, Y. Zhang, W. Xing, Q. Xue and Z. Yan, *J. Mater. Chem. A*, 2017, **5**, 15460–15485.
- 53 H. Olsson, D. O. Carlsson, G. Nyström, M. Sjödin, L. Nyholm and M. Strømme, *J. Mater. Sci.*, 2012, **47**, 5317–5325.
- 54 R. Pan, O. Cheung, Z. Wang, P. Tammela, J. Huo, J. Lindh, K. Edström, M. Strømme and L. Nyholm, *J. Power Sources*, 2016, **321**, 185–192.
- 55 A. Mihranyan, A. P. Llagostera, R. Karmhag, M. Strømme and R. Ek, *Int. J. Pharm.*, 2004, **269**, 433–442.
- 56 H. Hu, B. Guan, B. Xia and X. W. Lou, *J. Am. Chem. Soc.*, 2015, **137**, 5590–5595.
- 57 A. Mihranyan, *J. Appl. Polym. Sci.*, 2010, **119**, 2449–2460.
- 58 C. Zhang, J. Zhao, L. Zhou, Z. Li, M. Shao and M. Wei, *J. Mater. Chem. A*, 2016, **4**, 11516–11523.
- 59 T. Wang, S. Zhang, X. Yan, M. Lyu, L. Wang, J. Bell and H. Wang, *ACS Appl. Mater. Interfaces*, 2017, **9**, 15510–15524.
- 60 H. Liang, J. Lin, H. Jia, S. Chen, J. Qi, J. Cao, T. Lin, W. Fei and J. Feng, *J. Mater. Chem. A*, 2018, **6**, 15040–15046.
- 61 T. Brousse, D. Bélanger and J. W. Long, *J. Electrochem. Soc.*, 2015, **162**, A5185–A5189.
- 62 Y. Liu, N. Fu, G. Zhang, M. Xu, W. Lu, L. Zhou and H. Huang, *Adv. Funct. Mater.*, 2017, **27**, 1605307.
- 63 T. Li, G. H. Li, L. H. Li, L. Liu, Y. Xu, H. Y. Ding and T. Zhang, *ACS Appl. Mater. Interfaces*, 2016, **8**, 2562–2572.
- 64 H. Wu, Y. Zhang, W. Yuan, Y. Zhao, S. Luo, X. Yuan, L. Zheng and L. Cheng, *J. Mater. Chem. A*, 2018, **6**, 16617–16626.
- 65 Y. Ko, M. Kwon, W. K. Bae, B. Lee, S. W. Lee and J. Cho, *Nat. Commun.*, 2017, **8**, 536.
- 66 L. Huang, D. Chen, Y. Ding, S. Feng, Z. L. Wang and M. Liu, *Nano Lett.*, 2013, **13**, 3135–3139.
- 67 H. Wan, J. Liu, Y. Ruan, L. Lv, L. Peng, X. Ji, L. Miao and J. Jiang, *ACS Appl. Mater. Interfaces*, 2015, **7**, 15840–15847.
- 68 S. C. Sekhar, G. Nagaraju and J. S. Yu, *Nano Energy*, 2017, **36**, 58–67.
- 69 G. Nagaraju, S. Chandra Sekhar, L. Krishna Bharat and J. S. Yu, *ACS Nano*, 2017, **11**, 10860–10874.
- 70 X. Xu, J. Tang, H. Qian, S. Hou, Y. Bando, M. S. A. Hossain, L. Pan and Y. Yamauchi, *ACS Appl. Mater. Interfaces*, 2017, **9**, 38737–38744.
- 71 X. Dong, Z. Guo, Y. Song, M. Hou, J. Wang, Y. Wang and Y. Xia, *Adv. Funct. Mater.*, 2014, **24**, 3405–3412.
- 72 A. Hajian, S. B. Lindström, T. Pettersson, M. M. Hamed and L. Wågberg, *Nano Lett.*, 2017, **17**, 1439–1447.





Review

# Sustainable Porous Carbon Materials Derived from Wood-Based Biopolymers for CO<sub>2</sub> Capture

Chao Xu \* and Maria Strømme

Division of Nanotechnology and Functional Materials, Department of Engineering Sciences, Uppsala University, SE-75121 Uppsala, Sweden; maria.stromme@angstrom.uu.se

\* Correspondence: chao.xu@angstrom.uu.se

Received: 26 December 2018; Accepted: 11 January 2019; Published: 16 January 2019



**Abstract:** Porous carbon materials with tunable porosities and functionalities represent an important class of CO<sub>2</sub> sorbents. The development of porous carbons from various types of biomass is a sustainable, economic and environmentally friendly strategy. Wood is a biodegradable, renewable, sustainable, naturally abundant and carbon-rich raw material. Given these advantages, the use of wood-based resources for the synthesis of functional porous carbons has attracted great interests. In this mini-review, we present the recent developments regarding sustainable porous carbons derived from wood-based biopolymers (cellulose, hemicelluloses and lignin) and their application in CO<sub>2</sub> capture.

**Keywords:** CO<sub>2</sub> capture; porous carbon; wood-based biopolymer; cellulose; lignin

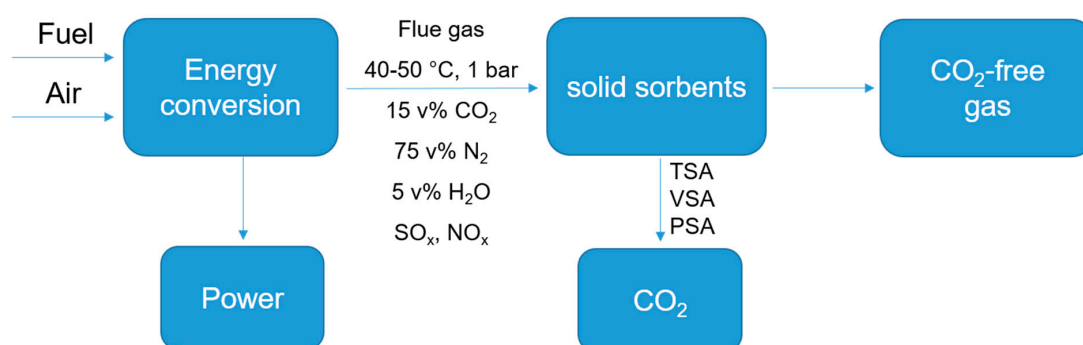
## 1. Introduction

CO<sub>2</sub> is the predominant greenhouse gas in the atmosphere. Because of the enormous combustion of fossil fuels during the last two centuries, the atmospheric CO<sub>2</sub> concentration has dramatically increased from its pre-industrial level of around 280 ppm to today's 408 ppm (December, 2018). According to a report by the Intergovernmental Panel on Climate Change (IPCC), the excess emission of CO<sub>2</sub> to the atmosphere is the main reason for the current global climate changes and associated problems, including global warming, sea level rise and ocean acidification, threatening human survival and development [1]. Hence, there is an urgent need for reducing the CO<sub>2</sub> emission and controlling the atmospheric CO<sub>2</sub> level to mitigate climate changes.

It is believed that fossil fuels will still dominate the global energy system in the foreseeable future. In this context, carbon capture and storage (CCS) is considered as a feasible and necessary approach to reduce CO<sub>2</sub> emission [2]. CCS covers a group of technologies including capture, compression, transportation and permanent storage of CO<sub>2</sub> [3]. Herein, CO<sub>2</sub> capture is the initial and the most important step. Conventional CO<sub>2</sub> capture processes address large CO<sub>2</sub> emission sources like flue gas emitted from coal-fired power plants, cement plants, oil refinery factories and iron and steel plants. Of the several technologies being developed for conventional CO<sub>2</sub> capture processes, post-combustion capture of CO<sub>2</sub> is a straightforward and commercially mature CO<sub>2</sub> capturing technique that can be easily retrofitted to existing power plants. It separates CO<sub>2</sub> from the flue gases, which consists of about 5–15 v% CO<sub>2</sub>, 70–75 v% N<sub>2</sub>, 5–7 v% H<sub>2</sub>O, 3–4 v% O<sub>2</sub>, and NO<sub>x</sub> and SO<sub>x</sub> with low concentrations (a few hundred ppm) [4]. The low pressure of the flue gases (ca. 1 atm) and their low CO<sub>2</sub> concentration require a high separation efficiency for CO<sub>2</sub> over other gas components at ambient pressure. Amine scrubbing, an absorption technique using aqueous alkanolamines solution to remove CO<sub>2</sub> from gas streams, has been applied industrially in natural gas purification and post-combustion capture of CO<sub>2</sub> for more than 50 years [5]. The chemical reaction of CO<sub>2</sub> with amine forms stable carbamates, offering a high efficiency for CO<sub>2</sub> capture and separation. However, it suffers from several drawbacks

of high energy penalties for the amine regeneration, risk of amine leakage and corrosion to the employed equipment.

Recently, large efforts have been devoted to the development of adsorption-driven separation techniques using porous materials as solid sorbents for CO<sub>2</sub> capture, which is considered an alternative approach to the amine scrubbing process [6–8]. Porous materials are a type of solid containing pores, usually interconnected, or channels possessing a high surface area [9]. Typical examples are traditional zeolites, activated carbons, mesoporous oxides and emerging metal-organic frameworks (MOFs), covalent-organic frameworks, porous organic polymers, etc. Different from the chemical absorption approach, a typical adsorption process starts by attracting CO<sub>2</sub> molecules onto the large surface of the porous solid by physisorption and/or chemisorption interactions. To regenerate the solid adsorbent and remove and concentrate the CO<sub>2</sub>, the CO<sub>2</sub>-filled solid is exposed to temperature, vacuum or pressure swing adsorption (TSA, VSA, PSA) cycles (Scheme 1) [10]. Because of the much weaker CO<sub>2</sub>-adsorbent interactions taking place in the above described process than in CO<sub>2</sub>-amine interactions/chemical reactions, the adsorption-driven separation technique requires significantly lower amounts of energy in the regeneration procedure compared with the amine-scrubbing process.



**Scheme 1.** Post-combustion capture of CO<sub>2</sub> from flue gas using solid sorbents. TSA = temperature swing adsorption; VSA = vacuum swing adsorption; PSA = pressure swing adsorption.

In general, CO<sub>2</sub> adsorption capacity mainly depends on intrinsic characteristics (e.g., surface area, pore size and adsorption sites) of the porous material, while the adsorption selectivity is influenced by molecular sieving, thermodynamic equilibrium and kinetic effect. Therefore, all of these factors have to be taken into account for the design and selection of porous materials as CO<sub>2</sub> adsorbents towards a high CO<sub>2</sub> adsorption capacity and a high adsorption selectivity of CO<sub>2</sub>-over-other gases (e.g., N<sub>2</sub>, H<sub>2</sub>O, CH<sub>4</sub>). Other factors such as cost, stability and processability of the material should also be considered when it comes to practical applications. For example, zeolites, crystalline microporous aluminosilicates, are widely used in industrial CO<sub>2</sub> capture. They usually display high CO<sub>2</sub> adsorption capacities and high CO<sub>2</sub>-over-N<sub>2</sub> selectivities because of their uniform and narrow pore sizes [11]. However, most zeolites are hydrophilic and drastically lose their adsorption capacity and selectivity for CO<sub>2</sub> under humid conditions. Therefore, the flue gas needs to be dried prior to passing through the zeolite sorbents for separating CO<sub>2</sub>, which significantly increase the operation cost. MOF materials are coordination polymers joining organic linkers and metal ions or clusters that have been intensively studied for CO<sub>2</sub> adsorption and separation. The use of reticular chemistry principles allows for the design of MOF materials at the molecular level with tailored crystal structure, pore size and functional groups for the development of highly efficient CO<sub>2</sub> sorbents [12,13]. However, MOF materials in this context suffer from low stability and high manufacturing cost. In comparison, porous carbons (or activated carbons) with high surface areas, tunable pore sizes and high tolerance to acidic, basic and humid environments are considered to be ideal sorbents for CO<sub>2</sub> capture [14,15]. More significantly, porous carbons can be prepared from sustainable biomass precursors providing an environmentally friendly and sustainable approach for the development of CO<sub>2</sub> sorbents [16].

Wood, the largest biomass resource on earth, has been used for tools, fuels and buildings throughout human history. Apart from these traditional functions, wood has been studied as a basis for functional materials during the development of modern material science and nanotechnology in recent years [17,18]. Cellulose, hemicellulose and lignin are biopolymers that constitute the main components of wood and many other plants. From a chemistry point of view, cellulose is a linear polysaccharide consisting of repeated D-glucose unit with the formula of  $(C_6H_{10}O_5)_n$ . Hemicellulose is a branched polysaccharide containing different sugar monomers. In comparison, lignin has a more complex composition and lacks a defined structure. It is basically an aromatic polymer network of cross-linked phenylpropane derived lignols. Because of their rich carbon content, natural abundance, and low cost, all these three biopolymers have been used as precursors to prepared porous carbons. This paper will review recent studies on sustainable porous carbon materials derived from the wood-based biopolymers cellulose, hemicellulose and lignin and their applications in CO<sub>2</sub> capture. The conversion route of biopolymers to porous carbons and the related mechanisms are introduced. The relationship between CO<sub>2</sub> adsorption behaviors (e.g., CO<sub>2</sub> adsorption capacity, CO<sub>2</sub>-over-N<sub>2</sub> selectivity, kinetics) and nanostructures (porosity, composition) of the biopolymer-based porous carbons are summarized. Additionally, we present our perspectives on the challenges and future developments of using sustainable porous carbon materials in CCS.

## 2. General Routes from Biomass to Porous Carbons

The conversion of biomass to porous carbons usually consists of two processes: carbonization and activation [19]. A conventional carbonization process is usually carried out in an inert atmosphere (e.g., N<sub>2</sub>, Ar) at elevated temperatures of 400–1000 °C, which is a typical pyrolytic approach. It involves several complex reactions such as dehydration, condensation and isomerization, by which most of the hydrogen and oxygen atoms are released from the biomass to form H<sub>2</sub>O, H<sub>2</sub>, CH<sub>4</sub>, CO gases and various volatiles while the carbon atoms are condensed as solid residues (usually denoted as char) with an increased carbon content [20]. The yield and carbon content of the solid are affected by several factors such as carbonization temperature, residence time, heating rate, chemical structure and thermal stability of the biomass. In general, an increased carbonization temperature and long residence time form chars with a reduced yield but elevated carbon content [21]. Apart from the conventional pyrolysis process, hydrothermal carbonization (HTC) is another approach that has been widely applied in the conversion of biomass to valuable carbon materials. The treatment of biomass under HTC conditions, usually at moderate temperatures (<300 °C) and self-generated pressures, forms hydrochars with increased C/H and C/O ratios and can be considered as an accelerated coalification process [22–25]. In contrast to the traditional pyrolytic carbonization method, the HTC process has several advantages. First, it operates under moderate temperatures, which significantly reduces the energy consumption. Second, wet biomass precursors do not need drying and can be directly subjected to the HTC treatment because the hydrothermal process takes place in water. In addition, the conversion of biomass by the HTC process gives carbon-rich hydrochars in high yields. Furthermore, the carbonaceous materials can be complexed with other components such as noble metal nanoparticles, magnetic nanoparticles, and electrochemically active species during the HTC process to form functional nanocomposites with desired nanostructures and compositions displaying a variety of physiochemical properties and functionalities. Therefore, the HTC method not only offers an energy-saving and environmentally friendly approach for biomass carbonization, but also significantly contributes to the development of carbon-based functional nanomaterials.

The chars obtained from the carbonization process are usually nonporous. Therefore, further activation, either physically or chemically, of the chars at elevated temperatures is a necessary step for the preparation of highly porous carbon materials. The physical activation method uses oxidizing atmosphere such as CO<sub>2</sub>, air or steam, while chemical activation applies activating agents such as KOH, NaOH, KHCO<sub>3</sub>, K<sub>2</sub>CO<sub>3</sub>, ZnCl<sub>2</sub> or H<sub>3</sub>PO<sub>4</sub> [26–28]. Certain moieties of the chars are prone to be oxidized and dehydrated by the oxidizing gases or chemical reagents during the activation process,

and thus, create rich micro- and mesopores [21]. The two activation methods produce porous carbons with large differences in porosity. In general, physical activation processes create porous carbons with moderate surface areas ( $<1000 \text{ m}^2/\text{g}$ ) and narrow micropores that can be beneficial for, e.g.,  $\text{CO}_2/\text{N}_2$  and  $\text{CO}_2/\text{CH}_4$  separation [29]. In contrast, chemical activation methods can significantly increase the surface area (up to  $>3000 \text{ m}^2/\text{g}$ ) and pore volume of the porous carbons that may be useful for applications in gas storage [30,31], water treatment [32,33], electrochemical supercapacitors [34,35], etc. In addition, chemical activation methods allow for conversion of biomass to highly porous carbons in a one-step carbonization/activation process, which greatly facilitates the manufacturing process without involving several procedures [36]. However, most chemical activation methods suffer from significant environmental disadvantages related to their dependence on large amounts of corrosive activating agents [37].

### 3. Synthesis of Porous Carbons from Wood-Based Biopolymers

Both traditional pyrolysis and hydrothermal treatment have been applied in the carbonization of wood-based biopolymers. The carbonization process and the obtained carbonaceous solid have been well studied with the assistance of various analytical techniques. For example, the combination of thermogravimetry (TG) and gas chromatography (GC)/mass spectrometry (MS) is useful to probe the pyrolysis behavior and analyze the gaseous products. Yang et al. have conducted TG analyses for cellulose, hemicellulose and lignin under  $\text{N}_2$  atmosphere [38]. These studies indicated that hemicellulose, having the lowest thermal stability among the three biopolymers because of its random amorphous structure and low molecular weight, starts to decompose at  $220 \text{ }^\circ\text{C}$ . Cellulose decomposes between  $315$  and  $390 \text{ }^\circ\text{C}$ . The relatively high thermal stability of cellulose can be attributed to its crystalline structures, strong hydrogen bonding between cellulose chains, and high molecular weight. In contrast, lignin has a wide and flat TG curve in the range of  $250$ – $900 \text{ }^\circ\text{C}$ . The slow pyrolysis rate and high thermal stability of lignin can be explained by its heavily cross-linked and aromatic-rich network. The solid yield of hemicellulose, cellulose and lignin at a temperature of  $900 \text{ }^\circ\text{C}$  was  $\sim 20\%$ ,  $7\%$  and  $40\%$ , respectively. The overall low solid yields can be attributed to the preferred gasification of the biopolymers at high temperatures with formation of rich gaseous products. Kwon et al. have studied the effects of gas atmosphere and heating rate on the pyrolytic carbonization of cellulose [39]. They showed that the use of different atmosphere ( $\text{N}_2$  and  $\text{CO}_2$ ) does not influence the solid yield at the same heating rate. However, the use of  $\text{CO}_2$  for the carbonization significantly enhanced the generation of gaseous products including  $\text{H}_2$ ,  $\text{CO}$  and  $\text{CH}_4$  because  $\text{CO}_2$  could promote the thermal cracking behaviors, which indicates that the use of  $\text{CO}_2$  as a reaction medium gave high thermal efficiency for biomass conversion. On the other hand, an increase of the heating rate from  $10 \text{ }^\circ\text{C}/\text{min}$  to  $500 \text{ }^\circ\text{C}/\text{min}$  reduced the solid yield from  $17\%$  to  $8\%$  at  $900 \text{ }^\circ\text{C}$ , which is consistent with the findings from other studies that a high heating rate usually leads to a low solid yield for biomass conversion. Deng et al. applied TG-MS tools to investigate the process of carbonization/activation of cellulose, hemicellulose and lignin in the presence of activating agent of  $\text{KHCO}_3$  [40]. The TG analysis showed that  $\text{KHCO}_3$  decomposed at  $200 \text{ }^\circ\text{C}$  and  $\text{KHCO}_3$  accelerated the pyrolysis of biopolymers. At temperatures above  $400 \text{ }^\circ\text{C}$ , the byproducts of  $\text{KHCO}_3$  (e.g.,  $\text{K}$ ,  $\text{K}_2\text{CO}_3$ , and  $\text{K}_2\text{O}$ ) catalyzed the activation process with the formation of  $\text{H}_2$  and  $\text{CH}_4$  as detected by MS. Based on these observations, this study proposed a possible structure evolution of the biopolymers during the carbonization/activation process, as shown in Figure 1. Interestingly, many studies have shown that cellulose can be transformed to porous carbons in a single step of carbonization under inert gas ( $\text{N}_2$  or  $\text{Ar}$ ) without the use of any oxidizing gases or activating agents. Bommier et al. synthesized a series of porous carbons with high surface areas by carbonization of filter paper under  $\text{Ar}$  atmosphere [41]. Based on TG-MS studies that monitored the carbonization process, they proposed a self-activation mechanism: the obtained carbon material was in-situ activated by the gaseous products (e.g.,  $\text{H}_2\text{O}$ ,  $\text{CO}_2$ ) from the decomposition of cellulose. The in-depth investigation of the thermal degradation process presented in these studies allows us to understand the conversion mechanisms and to optimize the carbonization parameters, such as

temperature, heating rate, residence time and atmosphere for the synthesis of carbon materials with desired properties.

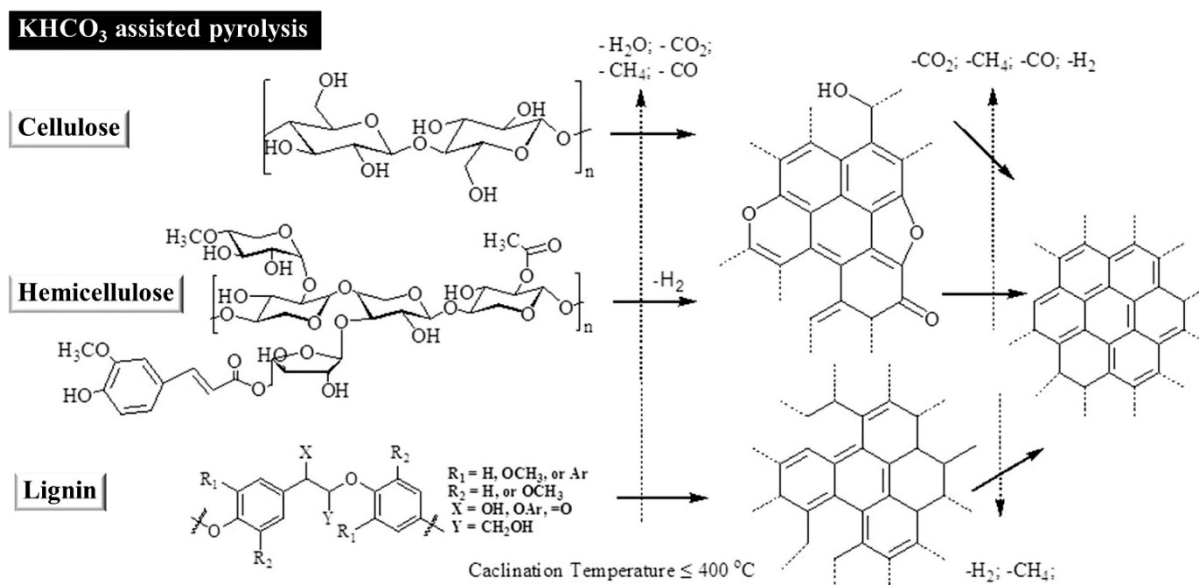


**Figure 1.** Possible carbonization routes of cellulose, hemicellulose and lignin in the presence of KHCO<sub>3</sub> (reproduced from [40], with permission from American Chemical Society, 2016).

As mentioned above, the HTC process has the advantage of operating at moderate temperatures, forming hydrochars with a rich variety of organic functional groups, allowing for the study of their molecular details by various spectroscopic and electron microscopic tools in order to investigate the details of the carbonization mechanism. Falco et al. have investigated the effects of processing temperature and time on morphology and chemical structure of the HTC hydrochars generated from cellulose [42]. X-ray diffraction, solid-state <sup>13</sup>C nuclear magnetic resonance (NMR) spectroscopy and scanning electron microscopy studies of the hydrochars revealed that the fibrous and crystalline structure of the cellulose was unaffected by hydrothermal treatment at low operating temperatures (<160 °C). Upon increasing the temperature, the fibrous structure started to decompose with formation of spherical particles. When the cellulose was treated at higher temperatures (200–280 °C), *sp*<sup>2</sup> hybridized carbons with moieties such as O=C=O, C=C–C were identified in the solid-state <sup>13</sup>C-NMR spectra of the obtained hydrochars. Based on these observations, two possible routes were proposed for the conversion of cellulose to hydrochars under HTC conditions (Figure 2). One route involved (a) hydrolysis of cellulose into glucose, (b) dehydration of glucose into hydroxymethylfurfural (HMF), (c) polymerization and polycondensation of HMF into polyfuranic chains, (d) intramolecular condensation, dehydration and decarboxylation of polyfuranic chains into aromatic rich carbon network via reactions. The other route was the direct aromatization of cellulose that forms aromatic carbon networks at higher HTC processing temperatures (200–280 °C); similar to a classical pyrolysis process. Other mechanistic routes have also been proposed for HTC conversion of various biopolymers by means of infrared, Raman and X-ray photoelectron spectroscopy [43–46]. These studies have greatly promoted the understanding of chemical reactions occurring during the HTC process, which enables tailoring of the nanostructure, porosity and functionality of carbon materials.

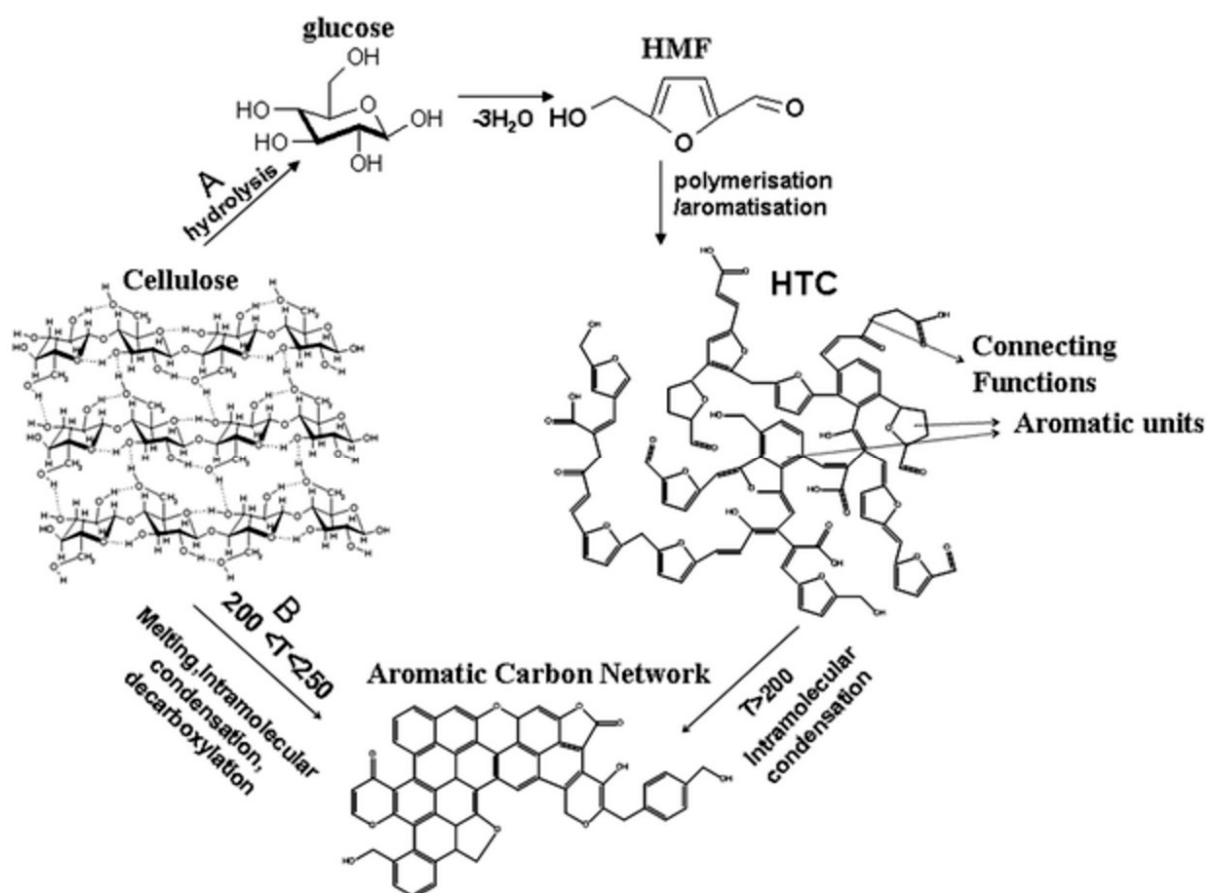


**Figure 2.** Conversion of cellulose to aromatic carbons under hydrothermal carbonization (HTC) conditions (reproduced from [22], with permission from The Royal Society of Chemistry, 2012).

#### 4. CO<sub>2</sub> Adsorption on Cellulose-, Hemicellulose- and Lignin-Derived Porous Carbons

As mentioned, cellulose can be converted to porous carbon material in a one-step pyrolytic carbonization process under N<sub>2</sub> or Ar atmosphere and physical or chemical activation of the carbonized solid could further increase its surface area and enhance its CO<sub>2</sub> adsorption capacity. For example, Heo et al. reported a series of porous carbons derived from commercial cellulose fibers in three steps: pre-pyrolysis under N<sub>2</sub> atmosphere at 200 °C, carbonization under N<sub>2</sub> atmosphere at 750–800 °C and physical activation with steam [47]. Morphology studies indicated that steam molecules played a key role in the pore-opening process and induced an increase in the surface area of the porous carbons formed. Meanwhile, the physical activation process significantly contributed to the evolution of ultramicropores (pore size < 0.8 nm). As a result, the surface areas were increased from 452–540 m<sup>2</sup>/g for pre-activated samples to 599–1018 m<sup>2</sup>/g for steam-activated samples. Accordingly, steam activation led to increase in CO<sub>2</sub> adsorption capacity and CO<sub>2</sub>-over-N<sub>2</sub> selectivities. Recently, we have applied *Cladophora* cellulose, a type of nanofibrous cellulose extracted from algae, and its chemically modified derivatives as precursors to prepare highly porous carbons [48]. The cellulose precursors were treated in a one-step carbonization/activation approach at 900 °C under N<sub>2</sub> or CO<sub>2</sub> atmosphere. The porous carbons activated in CO<sub>2</sub> had significantly higher surface areas (832–1241 m<sup>2</sup>/g) and higher volumes of ultramicropores (0.24–0.29 cm<sup>3</sup>/g) than those prepared in N<sub>2</sub> (393–500 m<sup>2</sup>/g; 0.11 cm<sup>3</sup>/g), due to the fact that CO<sub>2</sub> could activate the precursors to a higher extent than N<sub>2</sub> could, and hence, induce the formation of more (ultra-)micropores. As a result, the CO<sub>2</sub> adsorption capacity of the porous carbons was remarkably increased by the CO<sub>2</sub> activation approach. In another related study, Zhuo et al. prepared hierarchically porous carbons by carbonization/activation of cellulose aerogels under CO<sub>2</sub> and N<sub>2</sub> atmosphere, respectively [49]. The CO<sub>2</sub>-activated porous carbon had significantly higher

surface area, higher volume of micropores and higher CO<sub>2</sub> adsorption uptake than the N<sub>2</sub>-carbonized porous carbon. These results suggest that CO<sub>2</sub> or steam activation is an efficient approach to prepared cellulose-based porous carbons with high CO<sub>2</sub> adsorption capacities.

In comparison with physically activated carbons, chemically activated carbons have much higher surface areas, and thus, generally show relatively higher CO<sub>2</sub> adsorption capacities. For example, Sevilla et al. reported on chemical activation of hydrothermally carbonized cellulose by KOH [16]. The obtained microporous carbon had a very high surface area of 2370 m<sup>2</sup>/g and a relatively high CO<sub>2</sub> adsorption capacity of 5.8 mmol/g at 1 bar and 273 K. In addition, the carbon exhibited a high CO<sub>2</sub> adsorption rate and excellent adsorption recyclability. Wang et al. used hemp stem hemicellulose as precursor and prepared well-shaped porous carbon spheres by a HTC process and a subsequent KOH activation procedure. The obtained porous carbon spheres had large surface areas of up to 3062 m<sup>2</sup>/g and high CO<sub>2</sub> adsorption capacities of up to 5.63 mmol/g (1 bar, 273 K) [50]. Hao et al. reported on the treatment of lignin under HTC conditions at 360–385 °C. Further activation of the hydrocarbon by KOH gave highly porous carbons with surface areas of up to 2875 m<sup>2</sup>/g and high CO<sub>2</sub> adsorption capacities of up to 6.0 mmol/g (1 bar, 273 K) [51]. There are many activation parameters that influence the porosity and CO<sub>2</sub> adsorption behaviors of wood-biopolymer derived porous carbons. For example, Sangchoom et al. showed that activation at a high KOH/carbon ratio led to increase in the surface area and total pore volume for lignin-derived porous carbons; however, the CO<sub>2</sub> adsorption capacities and the ultramicropore volume decreased with increasing KOH/carbon ratio [52]. Balahmar et al. prepared lignin-based porous carbons by a novel mechanochemical activation method based on compaction of lignin precursors and KOH at a high pressure of 740 MPa prior to thermal activation. The compact contact between the lignin precursor and the activating agent resulted in enhanced surface area, pore volume and CO<sub>2</sub> adsorption capacity [53]. It should be noted that chemically activated carbons usually have broad pore size distributions and a high degree of mesoporosity. Therefore, their CO<sub>2</sub>-over-N<sub>2</sub> selectivities are largely sacrificed by the high surface areas.

Apart from surface area and pore volume, N-doping plays an important role in CO<sub>2</sub> adsorption for porous carbon materials. In order to investigate the effect of N-doping on CO<sub>2</sub> adsorption behaviors for cellulose-based porous carbons, Hu et al. prepared N-doped and N-free carbon aerogels by activation/carbonization of cellulose aerogels at high temperatures (700–900 °C) under NH<sub>3</sub> or N<sub>2</sub> atmosphere, respectively [54]. Notably, the N-doped carbon aerogel showed 40% higher CO<sub>2</sub> adsorption capacity than that of the N-free carbon aerogel (4.99 versus 3.56 mmol/g at 1 bar, 298 K). In addition, Demir et al. and Saha et al. prepared N-doped porous carbons from lignin. All these N-doped porous carbons showed relatively high CO<sub>2</sub> adsorption capacities up to 8.6 mmol/g (1 bar, 273 K) [55,56]. The high CO<sub>2</sub> adsorption capacity of the N-doped carbon materials can be explained by various interactions (e.g., Lewis acid-Lewis base interaction, hydrogen bonding interaction) between the N-containing species and the CO<sub>2</sub> molecules.

Besides using pristine biopolymers, there are some examples in the literature employing chemically modified biopolymers as precursors for the preparation of porous carbons. In a recent study, we reported chemical modification of *Cladophora* cellulose [48]. The pristine cellulose was first oxidized to dialdehyde cellulose (DAC) by using sodium metaperiodate as the oxidizing agent. The DAC was further reacted with chitosan, a biopolymer containing amine groups, to form a cross-linked cellulose (CLC) via polycondensation reactions. As a result, a series of porous carbons with tunable porosity were synthesized. Interestingly, the cross-linked structure in the cellulose precursor resulted in slightly decreased surface area, however, it created a high degree of ultramicropores in the obtained porous carbons. Hence, the CO<sub>2</sub> adsorption capacity (3.39 mmol/g for CLC-carbon versus 2.64 mmol/g for cellulose-carbon; 1 bar, 273K) and CO<sub>2</sub>-over-N<sub>2</sub> selectivity (42 for CLC-carbon versus 32 for cellulose-carbon; 273 K) were significantly increased. In addition, lignin can be also chemically modified to further increase the cross-linking. For example, Meng et al. reported hypercrosslinking of organosolv lignin with formaldehyde dimethyl acetal as crosslinker in a Friedel–Crafts reaction [57]. The obtained lignin had moderate CO<sub>2</sub> adsorption capacity but excellent CO<sub>2</sub>-over-N<sub>2</sub> selectivity.

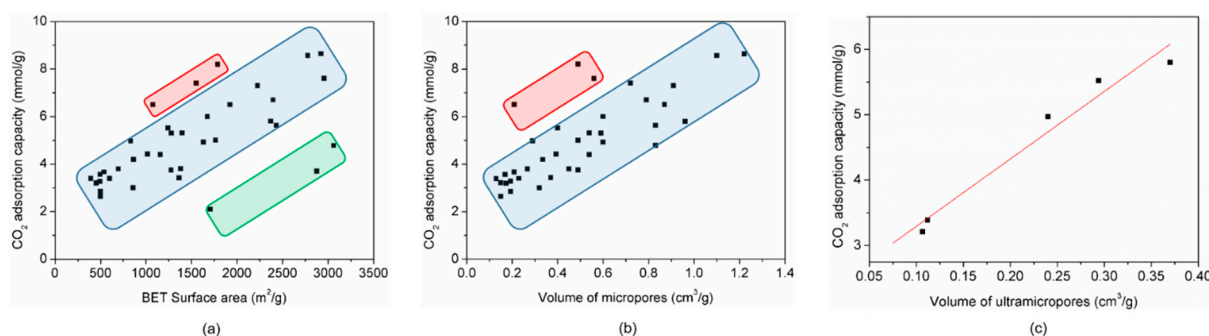
Pyrolysis of the hypercrosslinked lignin created microporous carbons with increased CO<sub>2</sub> capacity and relatively high selectivity. These studies demonstrate that introducing cross-linking structures into biopolymers can facilitate the formation of micropores in the derived carbon materials. Therefore, chemical modification of biopolymers allows us to tailor the precursor structures at the molecular level, and thus, to optimize the porosity and enhance the CO<sub>2</sub> capture efficiency for the corresponding porous carbon materials.

Table 1 lists literature reported cellulose-, hemicellulose- and lignin-derived porous carbons. Their activation method, surface areas, volume of (ultra-)micropores, CO<sub>2</sub> adsorption capacities at different partial pressures, CO<sub>2</sub>-over-N<sub>2</sub> selectivity and heat of adsorption ( $Q_{st}$ ) of CO<sub>2</sub> are summarized. For comparison, other selected sorbents of porous polymer, MOF and zeolite are also included. Based on these data, we have correlated the CO<sub>2</sub> adsorption capacity with surface area and pore volume of these biopolymer-derived porous carbons. Figure panels 3a and b show CO<sub>2</sub> uptake (1 bar, 273 K) versus Brunauer–Emmett–Teller (BET) surface area and CO<sub>2</sub> uptake (1 bar, 273 K) versus volume of micropores, respectively. Obviously, most of the data points in the two panels are confined within the blue narrow rectangular areas, indicating that there is a significant correlation between CO<sub>2</sub> uptake and surface area as well as between CO<sub>2</sub> uptake and micropore volume. However, the correlations are not strictly linear: for example, the data points in the green rectangle (Figure 3a) indicate that the corresponding porous carbons (MAC-S-8<sup>51</sup>, MAC-E-8<sup>51</sup>, HACS-5<sup>50</sup>.) have high surface areas but relatively low CO<sub>2</sub> uptakes. This can be attributed to the lack of ultramicropores in the porous carbons. In contrast, the data points in the red rectangles (Figure 3a,b) suggest that the corresponding carbon materials (LHPC-700<sup>55</sup>, LHPC-850<sup>55</sup>, LHPC-1000<sup>55</sup>, LAC2700<sup>52</sup>) have relatively high CO<sub>2</sub> adsorption capacities, although their surface areas and volumes of micropores are moderate. The relatively high CO<sub>2</sub> adsorption capacities can be attributed to the N-doped structures and the large volumes of ultramicropores. In addition, the plot of CO<sub>2</sub> uptake (1 bar, 273 K) versus volumes of ultramicropores in Figure 3c clearly demonstrates that the CO<sub>2</sub> uptake at 1 bar correlates strongly with the volume of ultramicropores, which is consistent with previous studies [58,59]. These results suggest that formation of large amounts of ultramicropores and N-doping structure in the porous carbons are efficient approaches to reach a high CO<sub>2</sub> adsorption capacity. Based on these reported data, it is estimated that 1 ton of biopolymer-based porous carbon could capture up to 50 kg of CO<sub>2</sub> at real conditions for postcombustion capture of CO<sub>2</sub> (0.15 bar, 40 °C) from flue gas. Apart from CO<sub>2</sub> adsorption capacity, CO<sub>2</sub>-over-N<sub>2</sub> selectivity and heat of adsorption ( $Q_{st}$ ) of CO<sub>2</sub> are both important for industrial CO<sub>2</sub> capture. Notably, the physically activated carbons have much higher CO<sub>2</sub>-over-N<sub>2</sub> selectivities (26–47) than those of the chemically activated carbons (5.4–25), because the former contain narrow (ultra-)micropores while the latter usually have broad pore size distributions and possess large amounts of meso- and macropores, and thus, reduce the molecular sieving effects. All these porous carbons have moderate  $Q_{st}$  (CO<sub>2</sub>) values of 20–41 kJ/mol, revealing that physical interactions govern the adsorption of the CO<sub>2</sub> molecules on the carbon materials. Compared to chemical adsorption, physical adsorption significantly speeds up the adsorption kinetics and facilitates regeneration of the sorbents under swing adsorption conditions [60].

**Table 1.** A summary of biopolymer-based porous carbons and their textural properties, CO<sub>2</sub> uptake, CO<sub>2</sub>/N<sub>2</sub> selectivity and heat of adsorption. Other selected sorbents (porous polymer, metal-organic frameworks (MOF), zeolite) are also included for comparison.

Sample	Biopolymer	Activating Agent	S <sub>BET</sub> (m <sup>2</sup> /g)	V <sub>micropores</sub> (cm <sup>3</sup> /g) <sup>a</sup>	CO <sub>2</sub> Uptake (mmol/g) <sup>b</sup>		S <sup>c</sup>	Q <sub>st</sub> (kJ/mol)	Ref.
					1 bar	0.15 bar			
CA800	Cellulose	N <sub>2</sub>	496	0.17	3.56	-	-	-	[54]
CF-700	Cellulose	N <sub>2</sub>	499	0.193	2.846	-	28.7	27.2	[47]
CF-750	Cellulose	N <sub>2</sub>	494	0.193	3.271	-	26.4	24.5	[47]
CF-800	Cellulose	N <sub>2</sub>	540	0.209	3.664	-	27.6	25.1	[47]
CF-850	Cellulose	N <sub>2</sub>	452	0.174	3.189	-	27.9	25.7	[47]
CF-700-act	Cellulose	CO <sub>2</sub>	599	0.229	3.395	-	35.1	29.5	[47]
CF-750-act	Cellulose	CO <sub>2</sub>	696	0.267	3.792	-	36.7	31.0	[47]
CF-800-act	Cellulose	CO <sub>2</sub>	863	0.334	4.192	-	47.1	37.8	[47]
CF-850-act	Cellulose	CO <sub>2</sub>	1018	0.393	4.416	-	39.2	33.4	[47]
LCN-1	Lignin	KOH	2922	1.22	8.64	3.2	-	40.0	[56]
LCN-2	Lignin	KOH	2779	1.10	8.56	3.03	-	32.5	[56]
LCN-3	Lignin	KOH	1631	0.60	4.92	1.88	-	41.0	[56]
L2600	Lignin	KOH	1277	0.59	5.3	1.3	-	-	[53]
L2600P	Lignin	KOH	2224	0.91	7.3	2.3	-	-	[53]
MAC-E-7	Lignin	KOH	1674	0.60	6.0	1.8	15.0	30.0	[51]
MAC-E-8	Lignin	KOH	2875	-	3.7	0.9	16.0	-	[51]
MAC-S-7	Lignin	KOH	1380	0.45	3.8	1.1	11.0	-	[51]
MAC-S-8	Lignin	KOH	1706	-	2.1	0.5	11.0	-	[51]
HACS-1	Hemicellulose	KOH	1276	0.49	3.75	0.68	-	-	[50]
HACS-2	Hemicellulose	KOH	1397	0.54	5.31	1.44	-	-	[50]
HACS-3	Hemicellulose	KOH	1764	0.49	5.00	1.37	-	-	[50]
HACS-4	Hemicellulose	KOH	2431	0.83	5.63	1.16	-	-	[50]
HACS-5	Hemicellulose	KOH	3062	0.83	4.78	0.85	-	-	[50]
LHPC-700	Lignin	KOH	1788	0.49	8.2	2.48	21.8	28.6	[55]
LHPC-850	Lignin	KOH	2957	0.56	7.6	2.26	15.6	28.4	[55]
LHPC-1000	Lignin	KOH	1075	0.21	6.5	2.07	13.5	27.3	[55]
PPC-850	Lignin	KOH	2396	0.79	6.7	1.97	10.8	27.6	[55]
Cell-N <sub>2</sub>	Cellulose	N <sub>2</sub>	859	0.32	3.00	0.82	-	-	[49]
Cell-CO <sub>2</sub>	Cellulose	CO <sub>2</sub>	1364	0.37	3.42	1.02	-	-	[49]
AC-4-700	Cellulose	KOH	2370	0.96 (0.37)	5.80	1.48	5.4	20.0	[16]
LAC2600	Lignin	KOH	1157	0.54	4.4	-	24.5	-	[52]
LAC2700	Lignin	KOH	1551	0.72	7.4	-	25.0	-	[52]
LAC2800	Lignin	KOH	1924	0.87	6.5	-	20.5	-	[52]
CC-AC-N <sub>2</sub>	cellulose	N <sub>2</sub>	500	0.15	2.64	1.30	32.6	31.5	[48]
DAC-AC-N <sub>2</sub>	Dialdehyde cellulose	N <sub>2</sub>	455	0.15 (0.11)	3.21	1.66	40.5	26.8	[48]
CLC-AC-N <sub>2</sub>	Cross-linked cellulose	N <sub>2</sub>	393	0.13 (0.11)	3.39	1.82	41.8	29.9	[48]
DAC-AC-CO <sub>2</sub>	Dialdehyde cellulose	CO <sub>2</sub>	1241	0.40 (0.29)	5.52	1.96	28.4	32.1	[48]
CLC-AC-CO <sub>2</sub>	Cross-linked cellulose	CO <sub>2</sub>	832	0.29 (0.24)	4.97	2.29	32.9	28.5	[48]
MOP A-B1			378	0.11	2.68	1.20	68	29.0	[61]
Cu-TDPAT			1938	0.93	10.1	2.60	300	42.2	[62]
Zeolite 13 <sup>d</sup>			616	0.34	4.80	3.50	-	-	[63]

<sup>a</sup> The values in the parentheses are volume of ultramicropores calculated from the N<sub>2</sub> adsorption isotherms; <sup>b</sup> data collected at 273 K; <sup>c</sup> Selectivity of CO<sub>2</sub>-over-N<sub>2</sub>; <sup>d</sup> CO<sub>2</sub> adsorption data was recorded at 288 K. (-): data not available.



**Figure 3.** Plots of (a) CO<sub>2</sub> uptake (1 bar, 273 K) versus BET surface area; (b) CO<sub>2</sub> uptake (1 bar, 273 K) versus volume of micropores; (c) CO<sub>2</sub> uptake (1 bar, 273 K) versus volumes of ultramicropores for cellulose-, hemicellulose- and lignin-derived porous carbons.

## 5. Conclusions and Perspectives

This review highlights the utilization of the wood-based biopolymers cellulose, hemicellulose and lignin as precursors to prepare sustainable and efficient porous carbons as CO<sub>2</sub> sorbents. Such porous carbons can be manufactured at large scale in low cost for practical industrial applications thanks to the abundance and low price of these biopolymers. The advantages of using such sustainable porous carbons for industrial CO<sub>2</sub> capture include high CO<sub>2</sub> adsorption capacity, high physiochemical stability, easy regeneration, fast adsorption/desorption rate, low operation cost and low manufacturing cost. However, most of these porous carbons have CO<sub>2</sub>-over-N<sub>2</sub> selectivities that are lower than those of other CO<sub>2</sub> sorbents, such as zeolite, MOFs and porous polymers. This limitation can be overcome by tailoring the nanostructures of the porous carbons, for example, by introducing hetero-atoms and CO<sub>2</sub>-philic species, formation of large amounts of narrow ultramicropores promoting the CO<sub>2</sub> adsorption kinetics and/or thermodynamics. Intensive studies have been devoted to tailoring the porosity of porous carbons by controlling the carbonization/activation conditions. However, the relationship between the molecular structure of the biopolymers and the properties of the porous carbons is still unrevealed. Future research could focus on such structure-property relationships in order to gain control over the properties of biopolymer-based porous carbons at the molecular level towards development of highly efficient CO<sub>2</sub> sorbents.

**Funding:** This research was funded by Stiftelsen ÅForsk (18-413).

**Conflicts of Interest:** The authors declare no conflict of interest.

## References

1. *Climate Change 2014: Synthesis Report. Contribution of Working Groups I, II and III to the Fifth Assessment Report of the Intergovernmental Panel on Climate Change*; IPCC: Geneva, Switzerland, 2014.
2. Haszeldine, R.S. Carbon Capture and Storage: How Green Can Black Be? *Science* **2009**, *325*, 1647. [[CrossRef](#)] [[PubMed](#)]
3. Gibbins, J.; Chalmers, H. Carbon capture and storage. *Energy Policy* **2008**, *36*, 4317–4322. [[CrossRef](#)]
4. D'Alessandro, D.M.; Smit, B.; Long, J.R. Carbon Dioxide Capture: Prospects for New Materials. *Angew. Chem. Int. Ed.* **2010**, *49*, 6058–6082. [[CrossRef](#)] [[PubMed](#)]
5. Rochelle, G.T. Amine scrubbing for CO<sub>2</sub> capture. *Science* **2009**, *325*, 1652–1654. [[CrossRef](#)] [[PubMed](#)]
6. Samanta, A.; Zhao, A.; Shimizu, G.K.H.; Sarkar, P.; Gupta, R. Post-Combustion CO<sub>2</sub> Capture Using Solid Sorbents: A Review. *Ind. Eng. Chem. Res.* **2012**, *51*, 1438–1463. [[CrossRef](#)]
7. Wang, Q.; Luo, J.; Zhong, Z.; Borgna, A. CO<sub>2</sub> capture by solid adsorbents and their applications: Current status and new trends. *Energy Environ. Sci.* **2011**, *4*, 42–55. [[CrossRef](#)]
8. Xu, C.; Hedin, N. Microporous adsorbents for CO<sub>2</sub> capture—A case for microporous polymers? *Mater. Today* **2014**, *17*, 397–403. [[CrossRef](#)]

9. Slater, A.G.; Cooper, A.I. Function-led design of new porous materials. *Science* **2015**, *348*, aaa8075. [[CrossRef](#)] [[PubMed](#)]
10. Hedin, N.; Andersson, L.; Bergström, L.; Yan, J. Adsorbents for the post-combustion capture of CO<sub>2</sub> using rapid temperature swing or vacuum swing adsorption. *Appl. Energy* **2013**, *104*, 418–433. [[CrossRef](#)]
11. Siriwardane, R.V.; Shen, M.-S.; Fisher, E.P. Adsorption of CO<sub>2</sub>, N<sub>2</sub>, and O<sub>2</sub> on Natural Zeolites. *Energy Fuels* **2003**, *17*, 571–576. [[CrossRef](#)]
12. Nugent, P.; Belmabkhout, Y.; Burd, S.D.; Cairns, A.J.; Luebke, R.; Forrest, K.; Pham, T.; Ma, S.; Space, B.; Wojtas, L.; et al. Porous materials with optimal adsorption thermodynamics and kinetics for CO<sub>2</sub> separation. *Nature* **2013**, *495*, 80–84. [[CrossRef](#)] [[PubMed](#)]
13. Mason, J.A.; Sumida, K.; Herm, Z.R.; Krishna, R.; Long, J.R. Evaluating metal-organic frameworks for post-combustion carbon dioxide capture via temperature swing adsorption. *Energy Environ. Sci.* **2011**, *4*, 3030–3040. [[CrossRef](#)]
14. Hao, G.-P.; Li, W.-C.; Qian, D.; Lu, A.-H. Rapid Synthesis of Nitrogen-Doped Porous Carbon Monolith for CO<sub>2</sub> Capture. *Adv. Mater.* **2010**, *22*, 853–857. [[CrossRef](#)] [[PubMed](#)]
15. Sevilla, M.; Valle-Vigón, P.; Fuertes, A.B. N-Doped Polypyrrole-Based Porous Carbons for CO<sub>2</sub> Capture. *Adv. Funct. Mater.* **2011**, *21*, 2781–2787. [[CrossRef](#)]
16. Sevilla, M.; Fuertes, A.B. Sustainable porous carbons with a superior performance for CO<sub>2</sub> capture. *Energy Environ. Sci.* **2011**, *4*, 1765–1771. [[CrossRef](#)]
17. Berglund Lars, A.; Burgert, I. Bioinspired Wood Nanotechnology for Functional Materials. *Adv. Mater.* **2018**, *30*, 1704285. [[CrossRef](#)]
18. Jiang, F.; Li, T.; Li, Y.; Zhang, Y.; Gong, A.; Dai, J.; Hitz, E.; Luo, W.; Hu, L. Wood-Based Nanotechnologies toward Sustainability. *Adv. Mater.* **2018**, *30*, 1703453. [[CrossRef](#)]
19. Dutta, S.; Bhaumik, A.; Wu, K.C.W. Hierarchically porous carbon derived from polymers and biomass: Effect of interconnected pores on energy applications. *Energy Environ. Sci.* **2014**, *7*, 3574–3592. [[CrossRef](#)]
20. Lin, J.-C.M. Development of a high yield and low cycle time biomass char production system. *Fuel Process. Technol.* **2006**, *87*, 487–495. [[CrossRef](#)]
21. Ioannidou, O.; Zabaniotou, A. Agricultural residues as precursors for activated carbon production—A review. *Renew. Sustain. Energy Rev.* **2007**, *11*, 1966–2005. [[CrossRef](#)]
22. Titirici, M.-M.; White, R.J.; Falco, C.; Sevilla, M. Black perspectives for a green future: Hydrothermal carbons for environment protection and energy storage. *Energy Environ. Sci.* **2012**, *5*, 6796–6822. [[CrossRef](#)]
23. Titirici, M.-M.; Antonietti, M. Chemistry and materials options of sustainable carbon materials made by hydrothermal carbonization. *Chem. Soc. Rev.* **2010**, *39*, 103–116. [[CrossRef](#)] [[PubMed](#)]
24. Titirici, M.-M.; White, R.J.; Brun, N.; Budarin, V.L.; Su, D.S.; del Monte, F.; Clark, J.H.; MacLachlan, M.J. Sustainable carbon materials. *Chem. Soc. Rev.* **2015**, *44*, 250–290. [[CrossRef](#)] [[PubMed](#)]
25. Hu, B.; Wang, K.; Wu, L.; Yu, S.-H.; Antonietti, M.; Titirici, M.-M. Engineering Carbon Materials from the Hydrothermal Carbonization Process of Biomass. *Adv. Mater.* **2010**, *22*, 813–828. [[CrossRef](#)] [[PubMed](#)]
26. Zhang, W.; Lin, N.; Liu, D.; Xu, J.; Sha, J.; Yin, J.; Tan, X.; Yang, H.; Lu, H.; Lin, H. Direct carbonization of rice husk to prepare porous carbon for supercapacitor applications. *Energy* **2017**, *128*, 618–625. [[CrossRef](#)]
27. Hayashi, J.I.; Kazehaya, A.; Muroyama, K.; Watkinson, A.P. Preparation of activated carbon from lignin by chemical activation. *Carbon* **2000**, *38*, 1873–1878. [[CrossRef](#)]
28. Carrott, P.J.M.; Ribeiro Carrott, M.M.L. Lignin—From natural adsorbent to activated carbon: A review. *Bioresour. Technol.* **2007**, *98*, 2301–2312.
29. Hao, W.; Björkman, E.; Lilliestråle, M.; Hedin, N. Activated carbons prepared from hydrothermally carbonized waste biomass used as adsorbents for CO<sub>2</sub>. *Appl. Energy* **2013**, *112*, 526–532. [[CrossRef](#)]
30. Zhang, F.; Ma, H.; Chen, J.; Li, G.-D.; Zhang, Y.; Chen, J.-S. Preparation and gas storage of high surface area microporous carbon derived from biomass source cornstalks. *Bioresour. Technol.* **2008**, *99*, 4803–4808. [[CrossRef](#)]
31. Sevilla, M.; Fuertes, A.B.; Mokaya, R. High density hydrogen storage in superactivated carbons from hydrothermally carbonized renewable organic materials. *Energy Environ. Sci.* **2011**, *4*, 1400–1410. [[CrossRef](#)]
32. Gonzalez-Serrano, E.; Cordero, T.; Rodriguez-Mirasol, J.; Cotoruelo, L.; Rodriguez, J.J. Removal of water pollutants with activated carbons prepared from H<sub>3</sub>PO<sub>4</sub> activation of lignin from kraft black liquors. *Water Res.* **2004**, *38*, 3043–3050. [[CrossRef](#)] [[PubMed](#)]

33. Phan, N.H.; Rio, S.; Faur, C.; Le Coq, L.; Le Cloirec, P.; Nguyen, T.H. Production of fibrous activated carbons from natural cellulose (jute, coconut) fibers for water treatment applications. *Carbon* **2006**, *44*, 2569–2577. [[CrossRef](#)]
34. Hao, P.; Zhao, Z.; Tian, J.; Li, H.; Sang, Y.; Yu, G.; Cai, H.; Liu, H.; Wong, C.P.; Umar, A. Hierarchical porous carbon aerogel derived from bagasse for high performance supercapacitor electrode. *Nanoscale* **2014**, *6*, 12120–12129. [[CrossRef](#)]
35. Zu, G.; Shen, J.; Zou, L.; Wang, F.; Wang, X.; Zhang, Y.; Yao, X. Nanocellulose-derived highly porous carbon aerogels for supercapacitors. *Carbon* **2016**, *99*, 203–211. [[CrossRef](#)]
36. Tay, T.; Ucar, S.; Karagöz, S. Preparation and characterization of activated carbon from waste biomass. *J. Hazard. Mater.* **2009**, *165*, 481–485. [[CrossRef](#)] [[PubMed](#)]
37. Maciá-Agulló, J.A.; Moore, B.C.; Cazorla-Amorós, D.; Linares-Solano, A. Activation of coal tar pitch carbon fibres: Physical activation vs. chemical activation. *Carbon* **2004**, *42*, 1367–1370. [[CrossRef](#)]
38. Yang, H.; Yan, R.; Chen, H.; Zheng, C.; Lee, D.H.; Liang, D.T. In-Depth Investigation of Biomass Pyrolysis Based on Three Major Components: Hemicellulose, Cellulose and Lignin. *Energy Fuels* **2006**, *20*, 388–393. [[CrossRef](#)]
39. Kwon, E.E.; Jeon, E.-C.; Castaldi, M.J.; Jeon, Y.J. Effect of Carbon Dioxide on the Thermal Degradation of Lignocellulosic Biomass. *Environ. Sci. Technol.* **2013**, *47*, 10541–10547. [[CrossRef](#)]
40. Deng, J.; Xiong, T.; Wang, H.; Zheng, A.; Wang, Y. Effects of Cellulose, Hemicellulose, and Lignin on the Structure and Morphology of Porous Carbons. *ACS Sustain. Chem. Eng.* **2016**, *4*, 3750–3756. [[CrossRef](#)]
41. Bommier, C.; Xu, R.; Wang, W.; Wang, X.; Wen, D.; Lu, J.; Ji, X. Self-activation of cellulose: A new preparation methodology for activated carbon electrodes in electrochemical capacitors. *Nano Energy* **2015**, *13*, 709–717. [[CrossRef](#)]
42. Falco, C.; Baccile, N.; Titirici, M.-M. Morphological and structural differences between glucose, cellulose and lignocellulosic biomass derived hydrothermal carbons. *Green Chem.* **2011**, *13*, 3273–3281. [[CrossRef](#)]
43. Sevilla, M.; Fuertes, A.B. Chemical and Structural Properties of Carbonaceous Products Obtained by Hydrothermal Carbonization of Saccharides. *Chem. Eur. J.* **2009**, *15*, 4195–4203. [[CrossRef](#)] [[PubMed](#)]
44. Baccile, N.; Laurent, G.; Babonneau, F.; Fayon, F.; Titirici, M.-M.; Antonietti, M. Structural Characterization of Hydrothermal Carbon Spheres by Advanced Solid-State MAS <sup>13</sup>C NMR Investigations. *J. Phys. Chem. C* **2009**, *113*, 9644–9654. [[CrossRef](#)]
45. Kang, S.; Li, X.; Fan, J.; Chang, J. Characterization of Hydrochars Produced by Hydrothermal Carbonization of Lignin, Cellulose, d-Xylose, and Wood Meal. *Ind. Eng. Chem. Res.* **2012**, *51*, 9023–9031. [[CrossRef](#)]
46. Sevilla, M.; Fuertes, A.B. The production of carbon materials by hydrothermal carbonization of cellulose. *Carbon* **2009**, *47*, 2281–2289. [[CrossRef](#)]
47. Heo, Y.-J.; Park, S.-J. A role of steam activation on CO<sub>2</sub> capture and separation of narrow microporous carbons produced from cellulose fibers. *Energy* **2015**, *91*, 142–150. [[CrossRef](#)]
48. Xu, C.; Ruan, C.-Q.; Li, Y.; Lindh, J.; Strømme, M. High-Performance Activated Carbons Synthesized from Nanocellulose for CO<sub>2</sub> Capture and Extremely Selective Removal of Volatile Organic Compounds. *Adv. Sustain. Syst.* **2018**, *2*, 1700147. [[CrossRef](#)]
49. Zhuo, H.; Hu, Y.; Tong, X.; Zhong, L.; Peng, X.; Sun, R. Sustainable hierarchical porous carbon aerogel from cellulose for high-performance supercapacitor and CO<sub>2</sub> capture. *Ind. Crop. Prod.* **2016**, *87*, 229–235. [[CrossRef](#)]
50. Wang, Y.; Yang, R.; Li, M.; Zhao, Z. Hydrothermal preparation of highly porous carbon spheres from hemp (*Cannabis sativa* L.) stem hemicellulose for use in energy-related applications. *Ind. Crop. Prod.* **2015**, *65*, 216–226. [[CrossRef](#)]
51. Hao, W.; Björnerbäck, F.; Trushkina, Y.; Oregui Bengoechea, M.; Salazar-Alvarez, G.; Barth, T.; Hedin, N. High-Performance Magnetic Activated Carbon from Solid Waste from Lignin Conversion Processes. 1. Their Use As Adsorbents for CO<sub>2</sub>. *ACS Sustain. Chem. Eng.* **2017**, *5*, 3087–3095. [[CrossRef](#)]
52. Sangchoom, W.; Mokaya, R. Valorization of Lignin Waste: Carbons from Hydrothermal Carbonization of Renewable Lignin as Superior Sorbents for CO<sub>2</sub> and Hydrogen Storage. *ACS Sustain. Chem. Eng.* **2015**, *3*, 1658–1667. [[CrossRef](#)]
53. Balahmar, N.; Mitchell, A.C.; Mokaya, R. Generalized Mechanochemical Synthesis of Biomass-Derived Sustainable Carbons for High Performance CO<sub>2</sub> Storage. *Adv. Energy Mater.* **2015**, *5*, 1500867. [[CrossRef](#)]

54. Hu, Y.; Tong, X.; Zhuo, H.; Zhong, L.; Peng, X.; Wang, S.; Sun, R. 3D hierarchical porous N-doped carbon aerogel from renewable cellulose: An attractive carbon for high-performance supercapacitor electrodes and CO<sub>2</sub> adsorption. *RSC Adv.* **2016**, *6*, 15788–15795. [[CrossRef](#)]
55. Demir, M.; Tessema, T.-D.; Farghaly, A.A.; Nyankson, E.; Saraswat, S.K.; Aksoy, B.; Islamoglu, T.; Collinson, M.M.; El-Kaderi, H.M.; Gupta, R.B. Lignin-derived heteroatom-doped porous carbons for supercapacitor and CO<sub>2</sub> capture applications. *Int. J. Energy Res.* **2018**, *42*, 2686–2700. [[CrossRef](#)]
56. Saha, D.; Van Bramer, S.E.; Orkoulas, G.; Ho, H.-C.; Chen, J.; Henley, D.K. CO<sub>2</sub> capture in lignin-derived and nitrogen-doped hierarchical porous carbons. *Carbon* **2017**, *121*, 257–266. [[CrossRef](#)]
57. Meng, Q.B.; Weber, J. Lignin-based Microporous Materials as Selective Adsorbents for Carbon Dioxide Separation. *ChemSusChem* **2014**, *7*, 3312–3318. [[CrossRef](#)] [[PubMed](#)]
58. Sevilla, M.; Parra, J.B.; Fuertes, A.B. Assessment of the Role of Micropore Size and N-Doping in CO<sub>2</sub> Capture by Porous Carbons. *ACS Appl. Mater. Interfaces* **2013**, *5*, 6360–6368. [[CrossRef](#)]
59. Presser, V.; McDonough, J.; Yeon, S.-H.; Gogotsi, Y. Effect of pore size on carbon dioxide sorption by carbide derived carbon. *Energy Environ. Sci.* **2011**, *4*, 3059–3066. [[CrossRef](#)]
60. Plaza, M.G.; García, S.; Rubiera, F.; Pis, J.J.; Pevida, C. Post-combustion CO<sub>2</sub> capture with a commercial activated carbon: Comparison of different regeneration strategies. *Chem. Eng. J.* **2010**, *163*, 41–47. [[CrossRef](#)]
61. Xu, C.; Hedin, N. Synthesis of microporous organic polymers with high CO<sub>2</sub>-over-N<sub>2</sub> selectivity and CO<sub>2</sub> adsorption. *J. Mater. Chem. A* **2013**, *1*, 3406–3414. [[CrossRef](#)]
62. Li, B.; Zhang, Z.; Li, Y.; Yao, K.; Zhu, Y.; Deng, Z.; Yang, F.; Zhou, X.; Li, G.; Wu, H.; et al. Enhanced Binding Affinity, Remarkable Selectivity, and High Capacity of CO<sub>2</sub> by Dual Functionalization of a rht-Type Metal–Organic Framework. *Angew. Chem. Int. Ed.* **2012**, *51*, 1412–1415. [[CrossRef](#)] [[PubMed](#)]
63. Chue, K.T.; Kim, J.N.; Yoo, Y.J.; Cho, S.H. Comparison of Activated Carbon and Zeolite 13X for CO<sub>2</sub> Recovery from Flue Gas by Pressure Swing Adsorption. *Ind. Eng. Chem. Res.* **1995**, *34*, 591–598. [[CrossRef](#)]



© 2019 by the authors. Licensee MDPI, Basel, Switzerland. This article is an open access article distributed under the terms and conditions of the Creative Commons Attribution (CC BY) license (<http://creativecommons.org/licenses/by/4.0/>).